The search for high-mass protostars with ALMA revealed up to kilo-parsec scales (SPARKS)

I. Indication for a centrifugal barrier in the environment of a single high-mass envelope

T. Csengeri[1], S. Bontemps[2], F. Wyrowski[1], A. Belloche[1], K. M. Menten[1], S. Leurini[3], H. Beuther[4], L. Bronfman[5], B. Commerçon[6], E. Chapillon[2, 7], S. Longmore[8], A. Palau[9], J. C. Tan[10, 11], and J. S. Urquhart[12]

(Affiliations can be found after the references)

ABSTRACT

The conditions leading to the formation of the most massive O-type stars, are still an enigma in modern astrophysics. To assess the physical conditions of high-mass protostars in their main accretion phase, here we present a case study of a young massive clump selected from the ATLASGAL survey, G328.2551-0.5321. The source exhibits a bolometric luminosity of $1.3 \times 10^4 L_\odot$, which allows us to estimate its current protostellar mass to be between ~11 and 16 $M_\odot$. We show high angular-resolution observations with ALMA reaching a physical scale of ~400 au. To reveal the structure of this high-mass protostellar envelope in detail at a ~0.17″ resolution, we use the thermal dust continuum emission and spectroscopic information, amongst others from the CO (J=3–2) line, which is sensitive to the high velocity molecular outflow, the SiO (J=8–7), and SO$_2$ (J=$8_{2,6} - 7_{1,7}$) lines tracing shocks along the outflow, as well as several CH$_3$OH and HC$_3$N lines that probe the gas of the inner envelope in the closest vicinity of the protostar. The dust continuum emission reveals a single high-mass protostellar envelope, down to our resolution limit. We find evidence for a compact, marginally resolved continuum source, which is surrounded by azimuthal elongations that could be consistent with a spiral pattern. We also report on the detection of a rotational line of CH$_3$OH within its v_t = 1 torsionally excited state. This shows two bright peaks of emission spatially offset from the dust continuum peak, and exhibiting a distinct velocity component ±4.5 km s^{-1} offset compared to the source v$_{lsr}$. Rotational diagram analysis and models based on local thermodynamic equilibrium (LTE) assumption require high CH$_3$OH column densities reaching N(CH$_3$OH)=$1.2 - 2 \times 10^{19}$ cm^{-2}, and kinetic temperatures of the order of 160-200 K at the position of these peaks. A comparison of their morphology and kinematics with those of the outflow component of the CO line, and the SO$_2$ line suggests that the high excitation CH$_3$OH spots are associated with the innermost regions of the envelope. While the HC$_3$N v_7 = 0 (J=37–36) line is also detected in the outflow, the HC$_3$N v_7 = 1e (J=38–37) rotational transition within the molecule's vibrationally excited state shows a compact morphology. We find that the velocity shifts at the position of the observed high excitation CH$_3$OH spots correspond well to the expected Keplerian velocity around a central object with 15 $M_\odot$ consistent with the mass estimate based on the source's bolometric luminosity. We propose a picture where the CH$_3$OH emission peaks trace the accretion shocks around the centrifugal barrier, pinpointing the interaction region between the collapsing envelope and an accretion disk. The physical properties of the accretion disk inferred from these observations suggest a specific angular momentum several times larger than typically observed towards low-mass protostars. This is consistent with a scenario of global collapse setting on at larger scales that could carry a more significant amount of kinetic energy compared to the core collapse models of low-mass star formation. Furthermore, our results suggest that vibrationally exited HC$_3$N emission could be a new tracer for compact accretion disks around high-mass protostars.

Key words. stars: massive – stars: formation – submillimeter: ISM

1. Introduction

Whether high-mass star formation proceeds as a scaled-up version of low-mass star formation is an open question in today's astrophysics. Signatures of infall and accretion processes associated with the formation of high-mass stars are frequently observed: ejection of material (Beuther et al. 2002; Zhang et al. 2005; Beltrán et al. 2011; Duarte-Cabral et al. 2013) with powerful jets (Guzmán et al. 2010; Moscadelli et al. 2016; Purser et al. 2016) and the existence of (massive) rotating structures, such as toroids and disks has been reported towards massive young stellar objects (MYSOs) (Beltrán et al. 2005; Sanna et al. 2015; Cesaroni et al. 2017). Most of these studies focus, however, on sources with high luminosities ($L_{\rm bol}$>3 × $10^4 L_\odot$), and are frequently associated with at least one embedded UC H II region (see also Mottram et al. 2011). Some of them harbour already formed O-type YSOs typically accompanied by radio emission and surrounded by hot molec-ular, as well as ionised gas. Some examples are G23.01-00.41 (Sanna et al. 2015), G35.20-0.74N (Sánchez-Monge et al. 2013a), and G345.4938+01.4677 (also known as IRAS 16562–3959, Guzmán et al. 2014) that have been studied in detail at high angular-resolution.

High-mass star formation activity is typically accompanied by the emergence of radio continuum emission (Rosero et al. 2016). The earlier evolutionary stage of high-mass star formation, that precedes the emergence of strong ionising radiation from an UC-H II region, is characterised by typically lower bolometric luminosity (e.g. Molinari et al. 2000; Sridharan et al. 2002; Motte et al. 2007). This stage can be considered as an analog of the Class 0 stage of low-mass protostars (Duarte-Cabral et al. 2013), which could be the main accretion phase, dominated by the cold and dusty envelope, and is accompanied by powerful ejection of material (Bontemps et al. 1996; André et al. 2000). Due to the high column densities, extinction

is very high towards these objects, and therefore high-mass protostars in this early stage are elusive (e.g. Bontemps et al. 2010; Motte et al. 2017). Rare examples of them are found to be single down to ∼500 au scales. They typically only probe a limited mass range: one of the best studied sources is the protostar CygX-N63 with a current envelope mass of ∼55 $M_\odot$ potentially forming a star with a mass of ≲20 $M_\odot$ (Bontemps et al. 2010; Duarte-Cabral et al. 2013).

We report here on the discovery of a *single high-mass protostellar envelope* with the largest mass observed so far, reaching the 100 $M_\odot$ mass range on 0.06 pc scale, and potentially forming a star with a mass of ∼50 $M_\odot$, corresponding to an O5-O4 type star. We resolve its immediate surroundings using high angular resolution observations reaching ∼400 au scale with the Atacama Large Millimeter/submillimeter Array (ALMA), which show evidence for a flattened, rotating envelope, and for accretion shocks implying the presence of a disk at a few hundred au scales.

2. Observations and data reduction

We study at high angular-resolution the mid-infrared quiet massive clump[1], G328.2551-0.5321, selected from the complete sample of such sources identified from the APEX Telescope Large Area Survey of the Galaxy (ATLASGAL) (Schuller et al. 2009; Csengeri et al. 2014, 2017a). The SPARKS project (Search for High-mass Protostars with ALMA up to kiloparsec scales, Csengeri et al., in prep, a) targets 35 of these sources corresponding to the early evolutionary phase of high-mass star formation (Csengeri et al. 2017b). Located at a distance of $2.5^{+1.7}_{-0.5}$ kpc , our target is embedded in the MSXDC G328.25-00.51 dark cloud (Csengeri et al. 2017a). We show an overview of the region in Fig. 1, left panel.

G328.2551-0.5321 has been observed with ALMA in Cycle 2, and the phase center was $(\alpha, \delta)_{J2000}$ = (15^{h}58^{m}00.05^s, −53°57′57″8). We used 11 of the 7 m antennas on the 2014 July 8 and 16, as well as 34 and 35 of the 12 m antennas on 2015 May 3, and 2015 September 1, respectively. The 7 m array observations are discussed in detail in Csengeri et al. (2017b). Here we also present the 12 m array observations, for which the baseline range is 15 m (17 kλ) to 1574 m (1809 kλ). The total time on source was 7.4 minutes, and the system temperature (T_{sys}) varies between 120 and 200 K.

The spectral setups used for the 7 m and 12 m array observations are identical, and the signal was correlated in low-resolution wide-band mode in Band 7, yielding 4 × 1.75 GHz effective bandwidth with a spectral resolution of 0.977 MHz which corresponds to ∼0.9 km s^{-1} velocity resolution. The four basebands were centred on 347.331, 345.796, 337.061, and 333.900 GHz, respectively.

The data have been calibrated in CASA 4.3.1 with the pipeline (version 34044). For the imaging, we used Briggs weighting with a robust parameter of −2, corresponding to uniform weighting, favouring a smaller beam size, and used the CLEAN algorithm for deconvolution. We created line-free continuum maps by excluding channels with line emission above $3\sigma_{rms}$ per channel determined on the brightest continuum source on the cleaned datacubes in an iterative process. The synthesised beam is 0.22″×0.11″ with 86° position angle measured from

north to east, which is the convention we follow from here on. The geometric mean of the major and minor axes corresponds to a beam size of 0.16″(∼400 au at the adopted distance for the source).

To create cubes of molecular line emission we subtracted the continuum determined in emission free channels around the selected line. To favour sensitivity, we used here a robust parameter of 0.5 for the imaging, which gives a synthesised beam of 0.34″×0.20″, corresponding, on average, to a 0.26″ resolution (∼650 au). For the SiO (8–7) datacube we lowered the weight on the longest baselines with a tapering function to gain in signal to noise. The resulting synthesised beam is 0.69″×0.59″(corresponding to ∼1600 au resolution).

We mainly focus here on molecular emission that originates from scales typically smaller than the largest angular scales of ∼ 7″, where the sensitivity of our 12 m array observations drops. The interferometric filtering has, however, a significant impact on both the continuum and the CO (3–2) emission, which are considerably more extended than the largest angular scales probed by the ALMA configuration used for these observations. For these two datasets, we therefore combine the 12 m array data with the data taken in the same setup with the 7 m array (Csengeri et al. 2017b). For this purpose we used the standard procedures in CASA for a joint deconvolution, and imaged the data with a robust parameter of −2 providing the highest angular resolution. The resulting beam is 0.23 × 0.12″with 86° position angle, with a geometric mean of 0.17″ for the continuum maps, and 0.31 × 0.18″with 88° position angle, with a geometric mean of 0.24″ for the CO (3–2) line. We measure an *rms* noise level in the final continuum image of ∼ 1.3 mJy/beam in an emission free region close to the centre on the image corrected for primary beam attenuation. The primary beam of the 12m array at this frequency is 18″5. We measure a $3\sigma_{rms}$ column density sensitivity of $2 - 8 \times 10^{23}$ cm^{-2} for a physically motivated range of plausible temperatures corresponding to $T_d = 30 - 100$ K, respectively, and within a beam size of 0.16″², and a 5σ mass sensitivity of 0.03–0.13 $M_\odot$ for the same temperature range.

3. Results

We discuss here the dust continuum image obtained with ALMA, which reveals a protostellar envelope that stays single down to our resolution limit of 400 au in physical scale (Sect. 3.1). We then report the detection of a high-energy rotational line of CH$_3$OH within its v_t = 1 torsionally excited state, and compare its observed properties with those of rotational CH$_3$OH lines within its v_t = 0 state (Sect. 3.2). We use then the local thermodynamic equilibrium (LTE) approximation to estimate the physical conditions of the CH$_3$OH emitting gas (Sect. 3.3). Finally, to constrain the origin of the CH$_3$OH emission, we compare it to other molecules, such as CO, SO$_2$ and HC$_3$N tracing outflowing gas associated with the protostellar activity (Sect. 3.4). The full view of the molecular complexity of this source will be discussed in a forthcoming paper (Csengeri et al. in prep, b).

---

[1] Mid-infrared quiet massive clumps are defined by weak or no emission in the 21−24 μm wavelength range. We follow here the definition of Csengeri et al. (2017a) which is based on Motte et al. (2007). As discussed there, our mid-infrared flux limit corresponds to that of an embedded star with $10^4 L_\odot$.

[2] We use $N(H_2) = \frac{F_\nu R}{B_\nu(T_d)\Omega \kappa_\nu \mu_{H_2} m_H}$ [cm^{-2}], where F_ν is the $3\sigma_{rms}$ flux density, $B_\nu(T)$ is the Planck-function, Ω is the solid angle of the beam calculated by $\Omega = 1.13 \times \Theta^2$, where Θ is the geometric mean of the beam major and minor axes; $\kappa_\nu = 0.0185$ g cm^{-2} including the gas-to-dust ratio, R, of 100; μ_{H_2} is the mean molecular weight per hydrogen molecule and is equal to 2.8; and m_H is the mass of a hydrogen atom.
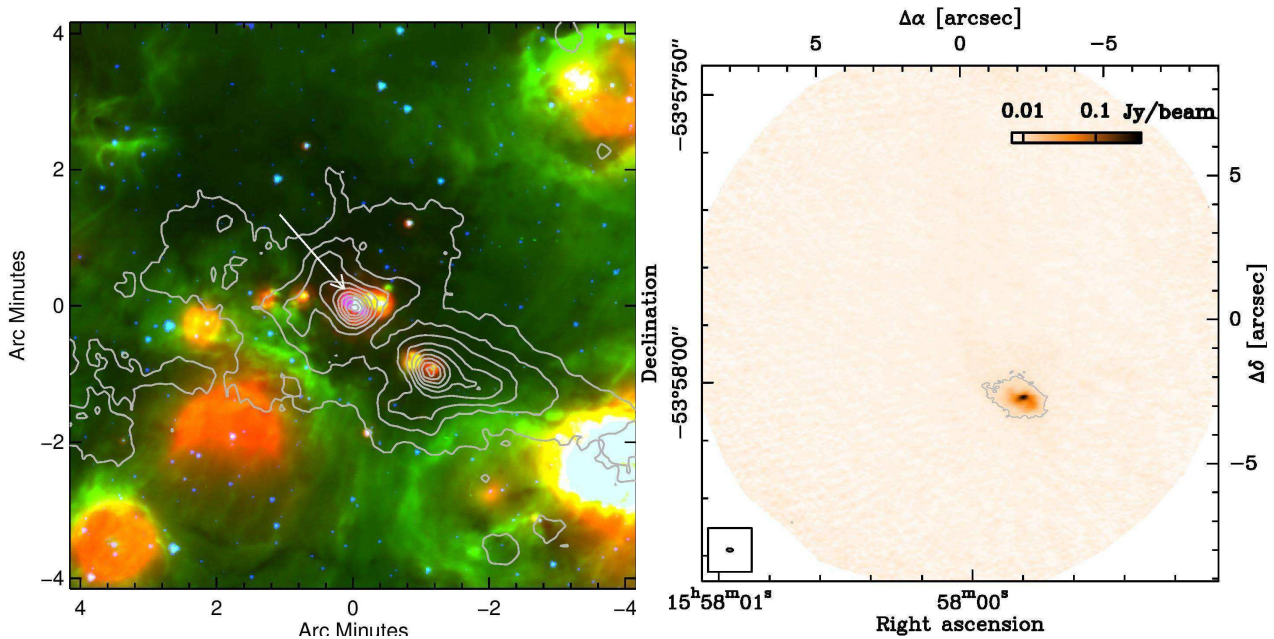
Fig. 1. Overview of the region centred on ℓ=+328.2551, b=−0.5321 in Galactic coordinates. *Left:* The three-color composite image is from the *Spitzer*/GLIMPSE (Benjamin et al. 2003) and MIPSGAL (Carey et al. 2009) surveys (blue: 4.5 μm, green: 8 μm, red: 24 μm) and is shown in Galactic coordinates. The contours show the 870 μm continuum emission from the ATLASGAL survey (Schuller et al. 2009; Csengeri et al. 2014). The arrow marks the dust continuum peak of the targeted clump. *Right:* Line-free continuum emission imaged at 345 GHz with the ALMA 12m array. The color scale is linear from −3σ to 120σ. The contour shows the 7σ level. The FWHM size of the synthesised beam is shown in the lower left corner.
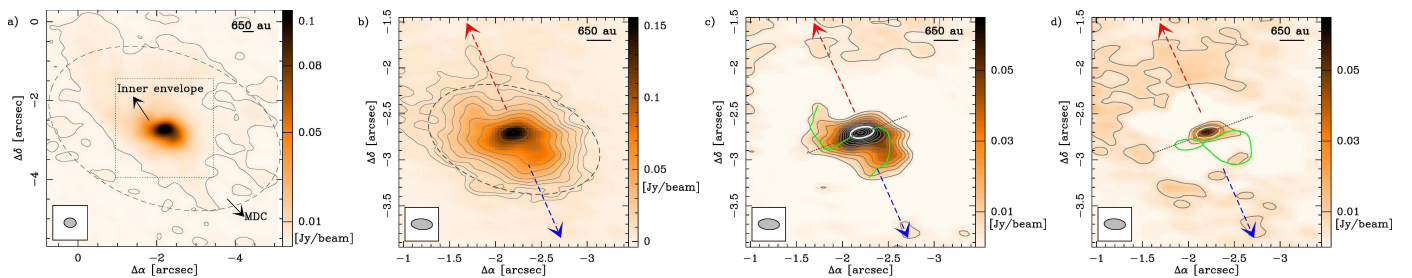
Fig. 2. A zoom on Fig. 1 of the protostar centred on $\Delta\alpha = -2.17''$, and $\Delta\delta = -2.76''$ offset from the phase center. *a)* Continuum emission smoothed to a resolution of 0.27″ showing the extended emission at the scale of the MDC. The color scale is linear between −1 and 105 mJy/beam, and the contour displays the 1.4 mJy/beam level corresponding to ∼5σ. Dashed ellipse shows the *FWHM* of the MDC from Table 1 adopted from Csengeri et al. (2017b). The region of the inner envelope shown in panels *b* to *c* is outlined by a dashed box. The *FWHM* beam is shown in the lower left corner of all panels. *b)* Line-free continuum emission in the original, unsmoothed 12m and 7m array combined map where the beam has a geometric mean of 0.17″. The color scale is linear between −3σ and 120σ, contours start at 7σ and increase on a logarithmic scale up to 120σ by a factor of 1.37. The red and blue dashed lines show the direction of the CO outflow (see Fig. 7 and Sect. 3.4). The dark gray dashed ellipse shows 2× the major and minor axes of the fitted 2D Gaussian. *c)* Residual continuum emission after removing a 2D Gaussian with a fixed lower peak intensity from the envelope component in order to enhance the contrast of the inner envelope. The color scale is linear from 0 to 50σ. The contours start at 3σ and increase by 6σ. White ellipse shows the *FWHM* of the fitted 2D Gaussian to the residual from panel *b*, and the green line outlines the azimuthal elongations. The black dotted line marks the direction perpendicular to the outflow. *d)* Residual continuum emission after removing the Gaussian fit to the envelope component (see the text for details). The color scale is the same as in panel *c*. Contours start at 5σ and increase by 10σ. Green contours show 80% of the peak of the velocity integrated emission of the 334.436 GHz $v_t = 1$ CH$_3$OH line shown in Fig. 4.

3.1. Dust continuum

### 3.1.1. A flattened envelope and a compact dust continuum source

We show the line-free continuum emission of G328.2551-0.5321 in Fig. 1, right panel, which reveals a single compact object down to 400 au physical scales. The source drives a prominent bipolar outflow (Sect. 3.4) suggesting that it hosts a protostar undergoing its main accretion phase. We resolve well the structure of the envelope, and show a zoom on the brightest region in Fig. 2a.

To extract the properties of the bulk emission of the dust, we use here a 2D Gaussian fit in the image plane as a first approach.

This reveals the position of the continuum peak at $(\alpha, \delta)_{J2000} = (15^h57^m59.802^s, -53°58'00.''51)$, which is −2.17″,−2.76″ offset from the phase centre, and gives a full-width at half-maximum (*FWHM*) of 0.96″×0.56″ with a position angle of 74°. We calculate the envelope radius as $R_{90\%}^{env} = 1.95 \times \Theta/\sqrt{8\ln2}$, where Θ is the beam deconvolved geometric mean of the major and minor axes *FWHM*. This gives a radius, $R_{90\%}^{env}$, of 0.59″ corresponding to 1500 au. In the following we refer to this component, thus the structure within 1500 au, as the inner envelope (Fig. 2b).

In order to investigate the structure of the inner envelope, we remove a low-intensity 2D Gaussian fit, i.e. allowing only positive residuals for the brightest, central structure (Fig. 2c). This

reveals azimuthal elongations exhibiting a warped S-shape connecting to the continuum peak.
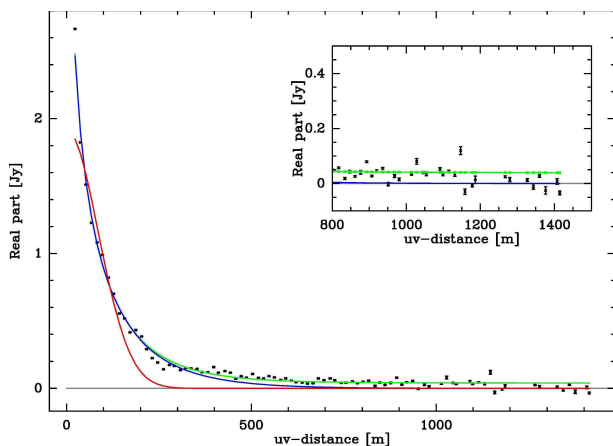
Fig. 3. Real part of the visibility measurements versus *uv*-distance shown for the ALMA 12 m array data. The data points show an average of line-free channels. The red and blue lines show fits to the envelope, an elliptic Gaussian, and a single component power-law fit, respectively. The green line shows a two component fit with a power-law and a compact disk source (see the text for more details).

3.1.2. A compact source within the envelope

When removing the bulk of the dust emission, i.e. our first 2D Gaussian fit to the envelope shown in Fig. 2*b*, we find a compact residual source with a peak intensity larger than 10σ in Fig. 2*d*. We determine its properties with another 2D Gaussian fit in the image plane data and identify a compact source that is resolved only along its major axis. The beam deconvolved $R_{90\%}^{disk}$ radius is ~0.1″, corresponding to an extent of 250 au. The properties and the corresponding flux densities of the inner envelope and the compact component based on our analysis in the image plane are summarised in Table 1.

These results suggest that the envelope itself is not well described by a Gaussian flux density distribution, and to test whether the residual source is better represented by a different flux density profile, we also perform a fitting procedure in the *uv*-domain. We fit the visibilities averaged over line-free channels as a function of *uv*-distance for the ALMA 12m array data (Fig. 3). We find that a single power-law component provides a relatively good fit to the data up to ~300 m long baselines. The visibility points show, however, a significant residual on the longer baselines further suggesting the presence of a compact component (see inset of Fig. 3).

We used various geometries to fit the compact component, however, we can only constrain that it is unresolved along its minor axis. Our models show that the compact source is consistent with a disk component with a flux density of 43 mJy, and a 0.2″ major axis *FWHM*. As a comparison, our analysis in the image plane attributes a somewhat larger flux density to this compact component, but finds a similar spatial extent. Later we argue that this component, that is significantly more compact than the in the inner envelope, likely corresponds to a compact accretion disk around the central protostar (Sect. 4.3).

3.1.3. The mass reservoir for accretion

To understand the distribution of dust emission on various scales, we compare the recovered emission from the 12 m array observations, the 12 m and 7 m array combined data, and the total flux density from the single dish observations from ATLASGAL. We recover a total flux density of 2.9 Jy in the field with the 12 m array observations only, which is a significant fraction (73%) of the ~4.0 Jy measured in the 7 m and 12 m array combined data. The 870 μm single-dish peak intensity measured on the ATLASGAL emission map is 10.26 Jy at this position, from which 8.32 Jy has been assigned to the clump in the catalog of Csengeri et al. (2014). This means that the 12m and 7m array combined observations recover ~50% of the total dust emission from the clump. Clearly, there is a large concentration of emission on the smallest scales which agrees with our previous results comparing the clump and the core scale properties in Csengeri et al. (2017a).

Based on this information, we describe the structure of the source in the following. We attribute the large scale emission to the clump, whose parameters are obtained from the ATLAS-GAL data at 0.32 pc scales (Fig. 1*a*). The smaller scale structure is attributed to a Massive Dense Core (MDC) forming a single protostellar envelope which has been first identified based on the ALMA 7m array observations in Csengeri et al. (2017b) at ~0.06 pc scales. In Fig 2*a*, in order to show the lower column density material at $N(H_2)$~ $2.5 - 10 \times 10^{22}$ cm^{-2} for $T = 30 - 100$ K, we smoothed the data to illustrate the extent of the MDC. The original, not smoothed ALMA 12 m and 7 m array combined data reveals the brightest emission with a 1500 au radius corresponding to the inner regions of the envelope showing the highest column densities.

Here, we attempt to provide a more robust mass estimate on the available mass reservoir for accretion based on the MDC properties within a radius of ~0.06 pc. To do this, we constrain the dust temperature (T_d) from a two component (cold and warm) greybody fit to the far-infrared spectral energy distribution (SED) (see App. A), where in particular the wavelengths shorter than 70 μm are a sensitive probe to the amount of heated dust in the vicinity of the protostar. From the fit to the SED we obtain a cold component at 22 K[3], and a warm component at ~48 K that we assign to the inner envelope. These models show, that the amount of warm gas is only a small fraction (< 5%) of the mass reservoir of the MDC. Adopting therefore, T_d =22 K for the MDC we obtain $M_{MDC} = 120\,M_\odot$[4]. Using a different dust emissivity (e.g. Peretto et al. 2013), and/or a gas-to-dust ratio of 150 would increase this value by 50-100%. The uncertainty in the distance estimation of this source would either decrease this value by 36%, or increase it by roughly a factor of three. On the measured physical sizes the effect of distance uncertainty is less dramatic, it would either decrease the inner envelope radius by 20% or increase it by 70%, if the source is located at the farthest likely distance.

Since the MDC is gravitationally bound, its mass should be available for accretion onto the central protostar. Assuming an efficiency of 20-40% (Tanaka et al. 2017), we can expect that an additional $24 - 48\,M_\odot$ could still be accreted on the protostar. Therefore, this makes our target one of the most massive protostellar envelopes known to date, which is likely in the process of forming an O-type star.

---

[3] In Csengeri et al. (2017a) we used T_d =25 K for all cores.

[4] We used Eq. 2 from Csengeri et al. (2017a) with the same parameters for the dust (dust emissivity, κ_ν = 0.0185 cm^2 g^{-1} from Ossenkopf & Henning 1994 accounting for a gas-to-dust ratio, R, of 100.)

Table 1. Dust continuum measurements.

| Component	Peak Intensity [Jy/beam]	Integrated flux d. [Jy]	$FWHM$ [$''\times''$]	p.a.[a]	Physical size	Used data
Clump	8.32	14.95	28.3$''\times$23.4$''$	$-31°$	0.32 pc	APEX/LABOCA[b]
MDC	2.10	4.0	6.1$''\times$3.85$''$	70°	0.06 pc	ALMA 7m array[c]
Inner envelope[d]	0.1	2.1	0.96$''\times$0.56$''$	74°	1500 au[e]	ALMA 7m+12m array
Residual (disk)[d]	0.063	0.068	0.26$''\times$0.12$''$	101°	250 au[e,f]	ALMA 7m+12m array

Notes.
[a] The position angle of the fitted Gaussian is measured from north to east.
[b] The corresponding parameters are extracted from the catalog of Csengeri et al. (2014) based on the ATLASGAL data.
[c] The listed parameters are from the ALMA 7 m array from Csengeri et al. (2017b).
[d] Parameters obtained with a 2D Gaussian fit in the image plane in this work.
[e] Corresponds to the beam deconvolved $R_{90\%}$, see the text for details. [f] This estimate is based on the resolved major axis.

Table 2. Summary of the molecular transitions studied in this work.

Molecule	Quantum number	Frequency [GHz]	Log_{10} Aij [s^{-1}]	E_{up}/k [K]	n_{cr}^a [cm^{-3}]	Database
$CH_3OH-A\ v_t = 0$	$2_{-2} - 3_{-1}$	335.13369	-4.57	45	1.1×10^7	CDMS
$CH_3OH-A\ v_t = 0$	$7_1 - 6_1$	335.58200	-3.29	79	3.6×10^7	CDMS
$CH_3OH-A\ v_t = 0$	$14_7 - 15_6$	336.43822	-4.25	488	6.7×10^5	CDMS
$CH_3OH-A\ v_t = 0$	$12_{-1} - 12_0$	336.86511	-2.84	197	1.0×10^8	CDMS
$CH_3OH-E\ v_t = 0$	$3_3 - 4_2$	337.13587	-4.61	62	6.9×10^7	CDMS
$CH_3OH-E\ v_t = 1$	3_0-2_1	334.42656	-4.26	315		CDMS
$CH_3OH-A\ v_t = 2$	$7_1 - 6_1$	336.60589	-3.79	747		JPL
$^{13}CH_3OH-A\ v_t = 0^c$	$12_{-1}-12_0$	335.56021	-3.40	193	1.0×10^8	CDMS
$^{13}CH_3OH-A\ v_t = 0^c$	$14_{-1}-14_0$	347.18828	-3.39	254	6.9×10^6	CDMS
$HC_3N\ v_7 = 0^b$	$37-36$	336.52008	-2.52	307		CDMS
$HC_3N\ v_7 = 1e$	$38-37$	346.45573	-2.48	645		CDMS
$SO_2\ v = 0$	$8_{2,6} - 7_{1,7}$	334.67335	-3.26	43	7.1×10^7	JPL
CO	$3 - 2$	345.79599	-3.61	33	4.00×10^4	CDMS

Notes.
[a] Calculated at $T = 100$ K using collisional rate coefficients from the LAMDA database (Schöier et al. 2005) where available.
[b] For HC_3N the molecular datafile lists cross sections up to $J_{\mathrm{up}} = 21$, and $T = 80$ K.
[c] Calculated from the collisional rate coefficients of the main isotopologue.
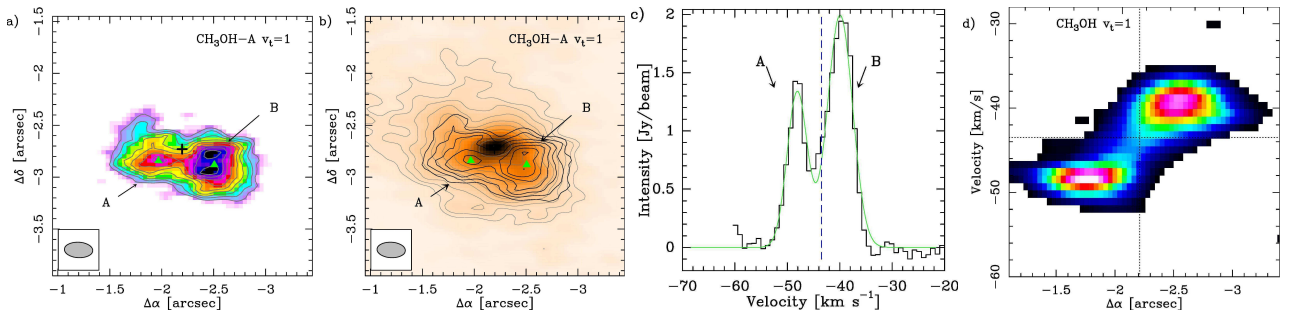
Fig. 4. *a)* Color scale shows the integrated intensity map of the $v_t = 1$ CH_3OH line at 334.4 GHz. The green triangles indicate the positions where the spectrum has been extracted for the rotational diagram analysis on the CH_3OH spots, and are labeled as A and B components. The black cross marks the position of the dust continuum peak. The beam is shown in the lower left corner. *b)* The color scale shows the continuum emission from Fig. 2b, contours and markers are the same as on panel *a*. *c)* Integrated spectrum of the torsionally excited CH_3OH transition at 334.4 GHz over the area shown in panel *a*. The green lines show the two component Gaussian fit to the spectrum. The blue dashed line shows the v_{lsr} of the source. *d)* Position-velocity diagram along the $\Delta\alpha$ axis and averaged over the shown extent of the cube corresponding to $\sim 2.5''$. The dotted lines mark the position of the dust peak and the v_{lsr} of the source.

3.2. Methanol emission

The total observed bandwidth of 7.5 GHz reveals emission from several molecular species. In this study we focus on a selected list of molecules summarised in Table 2. We first discuss the torsionally excited CH_3OH emission in Sect. 3.2.1, and to bet-

ter constrain its physical origin in Sect. 3.2.2 we discuss all unblended torsional ground state transitions of CH_3OH.
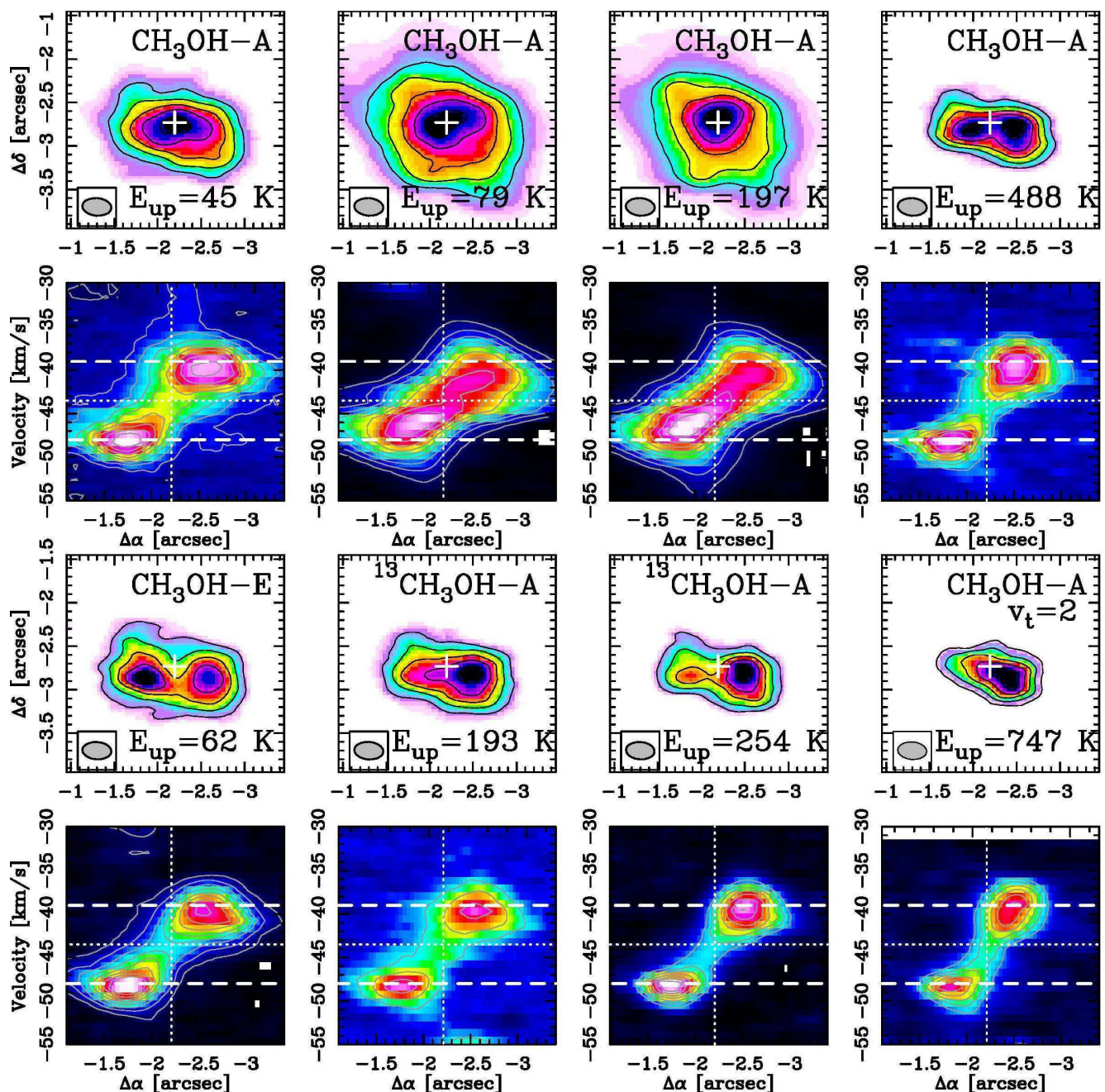
Fig. 5. CH$_3$OH 0th moment map and position velocity diagrams for the transitions listed in Table 2. The top row shows the 0th moment map calculated over a velocity range of [-55; -30] km s^{-1}, contours start at 30% of the peak and increase by 15%. White cross marks the position of the continuum peak. The beam is shown in the lower left corner. The symmetry of the methanol molecule is labeled on each panel, as well as the upper level energy of the transition. The subsequent row shows the position velocity map along the $\Delta\alpha$ axis and averaged over the shown extent of the cube corresponding to ~2.5″. The right-ascension offset of the continuum peak and the v_{lsr} velocity of the source are marked as white dotted line. Dashed lines show the $v_{lsr} \pm 4.5$ km s^{-1} corresponding to the peak velocity of the CH$_3$OH spots.

3.2.1. Torsionally excited methanol shows two bright spots offset from the protostar

Our continuous frequency coverage between 333.2 and 337.2 GHz, as well as between 345.2 and 349.2 GHz, includes several transitions of CH$_3$OH and its ^{13}C isotopologue. Most interestingly, towards the inner envelope, we detect and spatially resolve emission from a rotational transition of CH$_3$OH, from its first torsionally excited, $v_t = 1$, state at 334.42 GHz with an upper energy level of 315 K (Fig. 4a). Its spatial morphology shows two prominent emission peaks (marked as A and B in Fig. 4a), which spatially coincide with the azimuthal elonga-

tions within the envelope. The emission drops, however, significantly towards the continuum peak, i.e. the protostar (Fig. 4, *b*). We find that the observed morphology is dominated by two velocity components, which show an offset, on average, of -4.6, and $+3.6$ km s^{-1} compared to the v_{lsr} of the source[5] (Table 3). As discussed in Sect. 3.2.2, optical depth effects are unlikely to be at the origin of the observed velocity pattern. We spatially resolve the emission from these spots, and estimate the peak of its dis-

---

[5] We adopt the v_{lsr} of the dense gas seen on the clump/core scale used in Csengeri et al. (2017a).

Table 3. Observational parameters for the CH_3OH $v_t = 1$ lines, and results of the LTE modelling for CH_3OH.

	Observed parameters		LTE fit parameters		
	v_{lsr}^a	Δv	N	size	T_{ex}
	[km s^{-1}]	[km s^{-1}]	[cm^{-2}]	['']	[K]
A	-48.1 ± 0.1 (-4.6)	4.5 ± 0.2	1.6×10^{19}	0.4	160
B	-39.9 ± 0.1 ($+3.6$)	5.6 ± 0.1	2×10^{19}	0.4	170

Notes. [a] The number given in parenthesis corresponds to the difference between the line velocity and the -43.5 km s^{-1} v_{lsr} of the source.

tribution to fall between a projected distance of 300 and 800 au symmetric from the protostar.

The *pv*-velocity diagram along the $\Delta\alpha$ axis and averaged perpendicularly to this axis over the shown extent of $\sim 2.5''$ reveals that the emission is dominated by the two velocity components, and shows a pattern consistent with rotational motions (Fig. 4d). We compare these observations to simple models of the gas kinematics in more detail in Sect. 4.3.

3.2.2. Pure rotational lines of methanol

To further investigate the origin of the 334.426 GHz $v_t = 1$ methanol emission, in Fig. 5 we show maps of all the detected transitions of CH_3OH and its ^{13}C isotopologue in the torsional ground state, $v_t = 0$. They probe a range of upper energy levels between 45 K and 488 K, and based on our LTE modelling (Sect. 3.3.2) they are unlikely to be blended with emission from other species. We use these lines, in particular, to test whether a high optical depth toward the protostar could mimic the observed velocity pattern and morphology of the torsionally excited state line.

These maps reveal three transitions of the CH_3OH-A symmetry state with upper level energies of $E_{up} < 200$ K that peak on the continuum source, while its higher energy transitions show the two prominent peaks like the $v_t = 1$ CH_3OH line[6]. Our LTE modelling in Sect. 3.3.2, indeed shows that the three lowest energy transitions of CH_3OH-A have high optical depths.

The other transitions are, however, optically thin and they show two peaks of emission offset from the protostar similarly to the $v_t = 1$ CH_3OH line, while the emission drops towards the position of the protostar. In addition, their *pv*-diagrams are also similar to the $v_t = 1$ CH_3OH line revealing the two velocity components. Among these lines, we have the two $^{13}CH_3OH$ transitions detected with a high signal-to-noise ratio which are the least affected by optical depth effects. This leads us to conclude that the two prominent spots traced by the $v_t = 1$ state CH_3OH line cannot be a result of a large optical depth of CH_3OH towards the continuum peak.

We calculate the critical densities for these CH_3OH transitions in Table 2, and find that they all trace high density gas (if thermalised), strictly above 10^5 cm^{-3}, but typically on the order of 10^7 cm^{-3}. We notice that the different transitions have a varying contribution as a function of upper energy level from the central source, which suggests that they may trace two physical components, one associated with the inner envelope showing the bulk emission of the gas likely at lower temperatures, and another, warmer and denser component associated with the two peaks of the CH_3OH $v_t = 1$ line.

---

[6] The CH_3OH-E transitions in the band have an order of magnitude smaller Einstein coefficients which can explain why despite their lower energy level, all the CH_3OH-E lines show two peaks of emission.

3.3. Physical conditions of the methanol spots

We use here two methods to measure the physical conditions towards the methanol spots, and the position of the protostar as well. For this we extracted the spectrum covering the entire observed 7.5 GHz. To convert it from Jy/beam to K scales we used a factor of 198 K/Jy calculated for the 0.23'' averaged beam size at 335.2 GHz, and 347.2 GHz. Taking a mean conversion factor for the entire bandwidth adds less than 10% inaccuracy in the measurement of the brightness temperatures.

3.3.1. Rotational diagram analysis of CH_3OH transitions

We perform a rotational diagram analysis (Garay et al. 2010; Gómez et al. 2011) to estimate the rotational temperature of the CH_3OH emission, and its column density, $N(CH_3OH)$ at the CH_3OH peak positions indicated in Fig. 4, and towards the position of the protostar. We extracted the integrated intensities using a Gaussian fit to the CH_3OH transitions listed in Table 2. We include the $^{13}CH_3OH$ lines with an isotopic ratio of 60 (Langer & Penzias 1990; Milam et al. 2005), and exclude the 335.582 GHz and 336.865 GHz transitions from the fit. This is because as a combination of their large optical depths and interferometric filtering due to their spatial extent (see in Fig. 5) we observe considerably lower fluxes than expected if the CH_3OH emission is thermalised. For the rest of the transitions we assume optically thin emission. We show the rotational diagram in Fig. 6, where the error bars show the measured error on the Gaussian fit to the spectral lines, and are on the order of 10%. We obtain similar values for the two methanol peaks of $T_{rot} = 160 - 175$ K, and $N(CH_3OH) = \sim 8 \times 10^{18}$ cm^{-2}. The individual measurements have relatively large uncertainties, however, our results suggest that the two methanol spots have on the order of magnitude similar temperatures and column densities. Ignoring the effect of potentially more severe blending, we performed the same measurement on a spectrum extracted towards the continuum peak, which suggests similarly low rotational temperature as towards the brightest CH_3OH spot, and shows a somewhat lower column density of $N(CH_3OH) = \sim 7 \times 10^{18}$ cm^{-2}. While Fig. 5 suggests systematic differences in the CH_3OH emission between the high excitation CH_3OH spots and the continuum peak, the population diagram analysis shows that the three positions have similar column densities and rotational temperatures of methanol. This is particularly interesting since the radiation field, and hence the temperature is expected to be the strongest at the position of the protostar.

3.3.2. LTE modelling with WEEDs

Our observations cover a 7.5 GHz bandwidth, and the spectra extracted towards the CH_3OH peak positions show line forests of other molecular species, typically COMs. Therefore, to analyse the CH_3OH emission, we modelled the entire spectrum using the WEEDs package (Maret et al. 2011) assuming LTE conditions, which are likely to apply due to the high volume densities. The molecular composition of the gas towards the CH_3OH peaks will be described in a forthcoming paper, together with the detailed analysis.

In short, we performed the modelling in an iterative process, and started first with the CH_3OH lines. The input parameters are the molecular column density, kinetic temperature, source size, v_{lsr}, and line-width. From these parameters we fix the source size to 0.4'', which means that the emission is resolved, as it is suggested by the data (Fig. 5). The modelled transitions may have
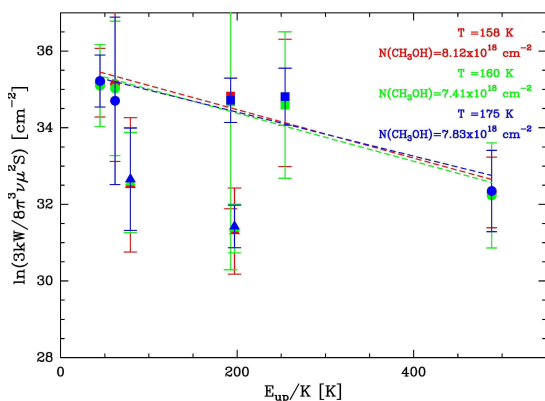
Fig. 6. Rotational diagram of the CH_3OH (and isotopologue) transitions from Table 2. The colours correspond to the measurements on different positions; green shows the position marked as A, red shows the position marked as B, and blue corresponds to the central position marked by a cross in Fig. 4. The filled circles show the CH_3OH lines, squares the $^{13}CH_3OH$ lines, and triangles the optically thick lines that are not used for the fit. The error bars show the linearly propagated errors from the Gaussian fit to the integrated intensities.

different source sizes, however, as long as they are resolved by our observations, the actual source size does not influence the result. The line-width of the CH_3OH line is obtained by the Gaussian fits to the extracted spectra. After obtaining a first, reasonably good fit to the listed CH_3OH transitions, we started to subsequently add other molecular species, mainly COMs that are responsible for the lower intensity lines (Csengeri et al in prep,b).

We created a grid of models for the CH_3OH column density, $N(CH_3OH)$, between 10^{17} and 10^{20} cm^{-2}, and kinetic temperatures between 50 and 300 K. We sampled by 25 linearly spaced values both parameter ranges, and then visually assessed the results. These models show that the detection or non detection of certain transitions allows us to put a rather strict upper limit on the kinetic temperature. Above $T_{kin} > 200$ K, our models predict that other transitions of the $v_t = 1$ state should be detectable at these column densities, the brightest ones are at 334.627 GHz ($J=22_{-3,0,1} - 22_{2,0,1}$), and 334.680 GHz ($J=25_{-3,0,1} - 24_{-2,0,1}$). Although these frequency ranges are affected by blending with COMs, models with $T_{kin} > 200$ K predict these rotational transitions within its $v_t = 1$ state to be brighter than the observed features in the spectrum at their frequency.

Our results give column densities on the order of $1.2-2\times10^{19}$ cm^{-2}, and a kinetic temperature around 160–200 K for the two positions. We find that the peak brightness temperatures for the transitions observed across the band are more sensitive to the methanol column density than to the variation in kinetic temperature. While this modelling takes into account blending with other transitions, our results are consistent with the estimates of column density and rotational temperature obtained from the rotational diagram analysis (Sect. 3.3.1).

3.4. Protostellar activity

3.4.1. Outflowing gas traced by the CO (J=3–2) line

The protostellar activity of the compact continuum source is revealed by a single bipolar molecular outflow shown in Fig. 7. The CO (3–2) line shows emission over a broad velocity range, Δv, of ± 50 km s^{-1} with respect to the source rest velocity (v_{lsr}) (Fig. 7a). Imaging the highest velocities of this gas reveals a single and confined bipolar molecular outflow. The orientation of

the high-velocity CO emission clearly outlines the axis of material ejection. The high velocity CO (3–2) emission coincides well with the integrated emission from the shock tracer SiO (8–7) (Fig. 7b), which likely traces the bow shocks along the outflow-axis (Fig. 7c).

In particular the brightest CO emission of the red-shifted northern lobe appears to be confined (Fig. 7c). Coinciding with the terminal position of the northern lobe, we detect emission at the source rest velocity of the shocked gas tracer, SiO (8–7), that is analogous to the bow-shocks observed in the vicinity of low-mass protostars. These indicate the shock front of the outflowing gas impacting the ambient medium.

Assuming that the maximum velocity observed in the CO (3–2) line corresponds to the speed at which the material has been ejected from the vicinity of the protostar, we can estimate when this material has been ejected. We measure an angular separation of $\sim 10''$ between the central object and the bow-shock seen in the SiO (8–7) line corresponding to a projected physical distance of 25000 au. Based on the observed line-wings of the CO (3–2) line, the measured velocity extent of the flow is ~ 50 km s^{-1}. We estimate an inclination angle, i, of 56°, where $i = 0°$ describes a face-on geometry, and $i = 90°$ corresponds to an edge-on view. This is obtained from the axis ratio of the measured envelope size from the dust emission assuming that it has a circular morphology[7]. After correcting for the projection effects, we obtain a dynamical age estimate of $t_{dyn} \sim 3.5 \times 10^3$ yr for the protostar. This estimate is, however, affected by the uncertainty of the inclination angle, and that of the jet velocity creating the bow shocks compared to the high velocity entrained gas seen by CO. While the jet velocity could be higher than traced by the entrained CO emitting gas leading to an even shorter time-scale, the highest velocities seen in CO may not reflect the expansion speeds of the outflow lobes as material accelerates. Considering the mass of the central object (Sect. 4.1) and the typically observed infall rates of the order of 10^{-3} $M_\odot$/yr (Wyrowski et al. 2012, 2016), the larger values of the age estimate, of the order of a few times 10^3 years to 10^4 years, seem the most plausible. This estimate, at the order of magnitude, supports the picture of the protostar being very young.

3.4.2. Sulphur-dioxide and cyanoacetylene

To understand the origin of the CH_3OH $v_t = 1$ line, we compare its distribution to other species, such as SO_2 and cyanoacetylene, HC_3N, in Fig. 8. Transitions from the latter species are detected both from the vibrational ground and excited states. These lines are not affected by blending, and probe various excitation conditions (see Table 2). It is clear that from the investigated molecules, the methanol emission corresponds the best to the distribution of the dust continuum; both SO_2 and HC_3N show a different morphology.

We show the SO_2 ($8_{2,6}-7_{1,7}$) line at 334.673 GHz which peaks on the position of the protostar and shows the most extended emission among the species discussed here, with a north-south elongation spatially coinciding with the outflow axis. Similarly, the HC_3N lines peak on the protostar. The $v_7=0$ ($J=37-36$) transition shows a north-south elongation following the outflow

---

[7] The outflow is rather confined with a small opening angle of $\sim$ 30°. Simple geometric considerations based on the outflow orientation, opening angle and the fact that there is no significant overlap along the line-of-sight between the blue and red shifted emission, we can exclude an inclination range between $i < 15°$, and $i > 75°$. An inclination angle range between 15° and 75° would result in $t_{dyn} = 6.3\times10^2 - 8.8\times10^3$ yr.
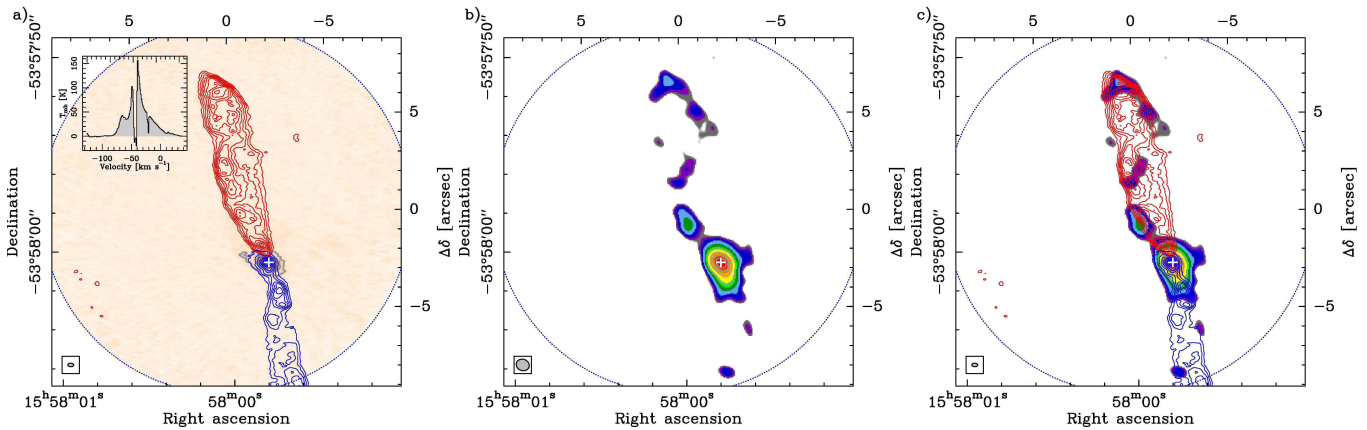
Fig. 7. *a)* Color scale shows the continuum emission from Fig. 1 panel *b*. The contours show the CO (3–2) integrated emission between −80 and −65 km s^{-1} for the blue, and between −30 and +36 km s^{-1} for the red, respectively. White cross marks the position of the dust continuum peak. The inset shows a spectrum of the integrated emission over the area of the lowest contours. *b)* The contours show the velocity integrated SiO (8–7) emission starting from 4σ (1σ=0.26 Jy/beam km s^{-1}), and increase by 2σ levels. *c)* Overlay of the CO (3–2) contours on the velocity integrated SiO (8–7) emission shown in panel *b*. The beam is shown in the lower left corner of each panel. On panel *c* it corresponds to that of the CO (3–2) map.
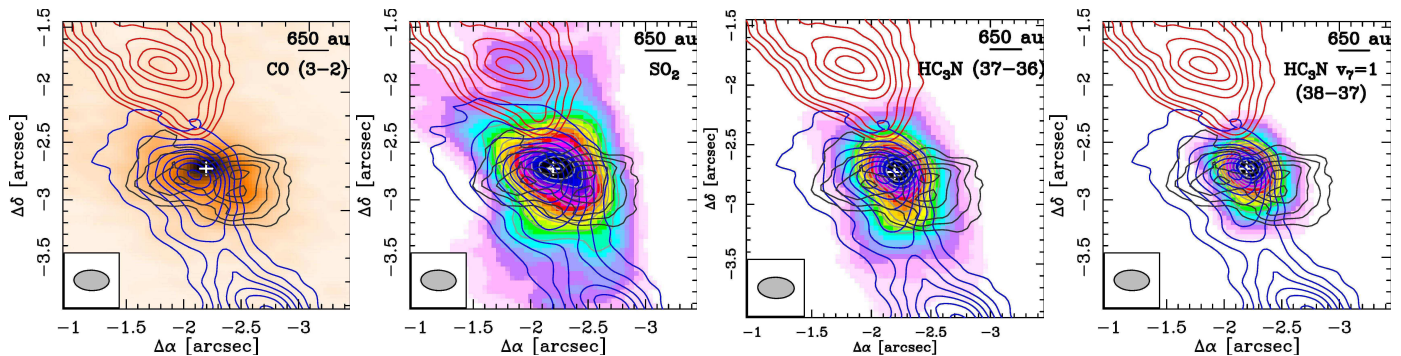
Fig. 8. A zoom on the envelope showing the CO (3–2) outflow lobes indicated in blue and red contours, the CH$_3$OH v_t = 1 line in black contours. The background shows the dust continuum, and moment 0 maps calculated over a velocity range of −55 to −35 km s^{-1} of SO$_2$, HC$_3$N (*J*=37-36), and HC$_3$N v_7 = 1 (*J*=38-37) from left to right, respectively. White cross marks the position of the dust continuum peak. The beam of the CO (*J*=3–2) data is shown in the lower left corner.

axis, and is more compact compared to the SO$_2$ line. The higher excitation state v_7=1 (*J*=38–37) transition also shows a north-south elongation along the outflow; it is, however, even more compact than the vibrational ground state line.

In Fig. 9 we show horizontal and vertical averages of the datacubes as a function of velocity (*pv*-diagrams). Due to the relatively simple source geometry, we show the averages along $\Delta\alpha$ and $\Delta\delta$ axes. For the CO emission we use the cube covering the primary beam, while for the other species we only use the region shown in Fig. 8. The high-velocity outflowing gas is clearly visible in the CO (3–2) line, and the kinematic pattern of both the SO$_2$, and HC$_3$N v_7 = 0 lines confirms that they show emission associated with the outflowing molecular gas. The velocity range of the HC$_3$N v_7 = 1 emission is clearly broader than that of the CH$_3$OH lines; it is, however not as broad as the SO$_2$, and HC$_3$N v_7 = 0 emission. The emission around $v_{lsr} \sim -33$ km s^{-1} close to the HC$_3$N v_7 = 1 line is a contamination from COMs with line forests, such as acetone and ethylene glycol.

4. Discussion

We identify a single high-mass protostellar envelope within the ∼600 $M_\odot$ mid-infrared quiet clump, G328.2551-0.5321. In Sect. 4.1 we argue that the protostar is still in its main accre-

tion phase, resembling the Class 0 phase of low-mass protostars (c.f. Duarte-Cabral et al. 2013). We investigate the origin of the CH$_3$OH emission in Sect. 4.2 and propose that in particular the torsionally excited state line traces shocks due to the infall from the envelope to an accretion disk. In Sect. 4.3 we compare its kinematics with a vibrationally excited state transition of HC$_3$N, that we propose as a potential new tracer for the accretion disk.

4.1. The most massive envelope of a young protostar

A luminosity of $L_{bol} = 1.3 \times 10^4 L_\odot$ (see App. A) associated with a massive envelope, and a strong outflow point to a still strongly accreting, young massive protostar. Due to the high extinction towards the protostar, we use evolutionary diagrams (Fig. 10) based on protostellar evolution models (Hosokawa & Omukai 2009) to estimate the mass of the central object.

According to models of protostellar evolution the observed luminosity is too high to originate only from accretion (Hosokawa et al. 2010), instead it is rather dominated by the Kelvin-Helmholtz gravitational contraction of the protostellar core. Using the typical accretion rate observed towards high-mass protostars and YSOs, i.e. of the order of $10^{-3} M_\odot$ yr^{-1} (Wyrowski et al. 2016), the Hosokawa tracks indicate that the protostar has to be bloated, and close to the maximum of
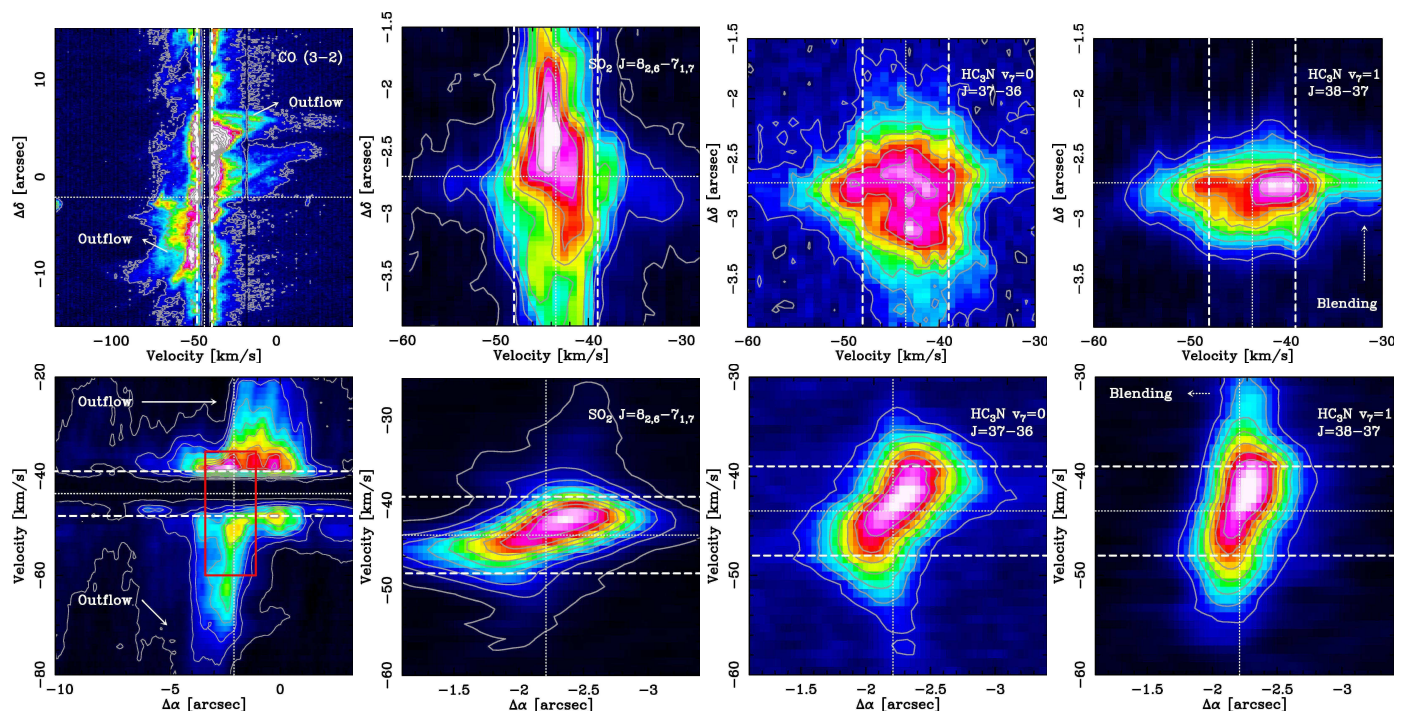
Fig. 9. Position-velocity (*pv*) diagrams along the $\Delta\delta$ axis and averaged over the shown extent of the cube (top row) and along the $\Delta\alpha$ axis (bottom row) of the CO (3–2), SO$_2$, HC$_3$N (J=37-36), and HC$_3$N v_7 = 1 (J=38-37) transitions from left to right, respectively. The dotted lines show the v_{lsr} of the source, and the position of the dust continuum peak. The dashed lines indicate velocities of $v_{lsr}\pm4.5$ km s^{-1} roughly corresponding to the velocities of the CH$_3$OH peaks. The red rectangle on the lower left panel corresponds to the region shown in the other panels. The contours start at 20% of the peak and increase by 10%, except for the panel of the CO and SO$_2$ lines, where the lowest contours start at 5% of the peak.

its radius during its protostellar evolution, suggesting that it is at the onset of the Kelvin-Helmholtz contraction phase (Hosokawa et al. 2010). During this regime, the luminosity does not depend strongly on the actual accretion rate and mainly depends on the mass of the protostar.

Using these models for the typically expected accretion rate of $\dot{M}_{acc} = 10^{-3}$ $M_\odot$ yr^{-1}, we find a central mass around 11 $M_\odot$ for $L_{bol} = 1.3 \times 10^4$ $L_\odot$. Evolutionary tracks with accretion rates of $\dot{M}_{acc} = 1 - 30 \times 10^{-4}$ $M_\odot$ yr^{-1} give a similar protostellar mass range, between 11.1 and 15.2 $M_\odot$, respectively. The protostellar radius adjusts, roughly in a proportional way, to the average accretion rate with a range of radius from 8 to 260 $R_\odot$ for $\dot{M}_{acc} = 1 - 30 \times 10^{-4}$ $M_\odot$ yr^{-1}. We can therefore assume that the current protostellar mass is relatively well determined, and lies in the range between 11 and 16 $M_\odot$. Taking the dynamical age estimate from Sect. 3.4.1 and the current propostellar mass, we can put an upper limit on the accretion rate by $\dot{M}_{acc} = M_{proto}/\tau_{dyn}$, which is between 3.1×10^{-3} and 4.2×10^{-3} $M_\odot$/yr. This estimate is, however considerably affected by the uncertainties in the dynamical age estimate (see Sect. 3.4.1).

Several types of maser emission also support the presence of an already high-mass protostellar object; the evolutionary models indicate, however, that due to the bloating of the protostar no strong ionising emission is expected despite its high mass. This is consistent with the lack of radio continuum detection towards this object. The field has been covered at 3.6 and 6 cm by a radio survey of southern Red MSX Sources (RMS) (Urquhart et al. 2007; Lumsden et al. 2013) that targeted a nearby MYSO/UCHII region only showing radio emission 1.1′ offset compared to our position. Similarly, radio continuum observations at 8.4 GHz only report a 4σ upper limit of 0.6 mJy (Phillips et al. 1998). Based on this upper limit and adopting a spherical model of ionised plasma with typical val-

ues of T_e=10^4 K electron temperature, EM=10^8 – 10^{10} pc cm^{-6} emission measure, we find that only a very compact H II region with a radius of 100 au could have remained undetected in these observations. This is an independent confirmation for the young nature of the protostar.

Based on the estimated current core mass of 120 $M_\odot$, we may expect a final stellar mass of ~50 $M_\odot$ (Fig. 10). The protostar of G328.2551-0.5321 is therefore a particularly interesting object, and we suggest that it is one of the rare examples of a bloated, high-mass protostar, precursor of a potentially O4-O5 stellar type star. There are only very few candidates of such bloated protostars in the literature (e. g. Palau et al. 2013, and references therein), and most of them correspond to objects detected in the optical, and the source presented here is much more embedded.

Throughout this work we refer to the continuum peak as a single high-mass protostellar envelope. However, we can not exclude that the source would be fragmented at smaller, i.e. <400 au scales which would lead to the formation of a close binary from a single collapsing envelope. While O-type stars have a high multiplicity (e. g. Sana 2017), we do not find any clear evidence at the observed scales that would hint to multiplicity on smaller scales. For example, the small outflow opening angle could suggest that either the system is still young, or there is a single source driving the outflowing gas. Alternatively, gravitational fragmentation of the massive inner envelope could lead to the formation of companions at a subsequent evolutionary stage.

4.2. Accretion shocks at the inner envelope

All CH$_3$OH lines follow the extension of the envelope, and their *pv*-diagrams are consistent with rotational motions (Fig. 5). Fig. 11 shows the contours of the CH$_3$OH v_t = 1 line in different velocity channels, and reveals a clear velocity gradient over the
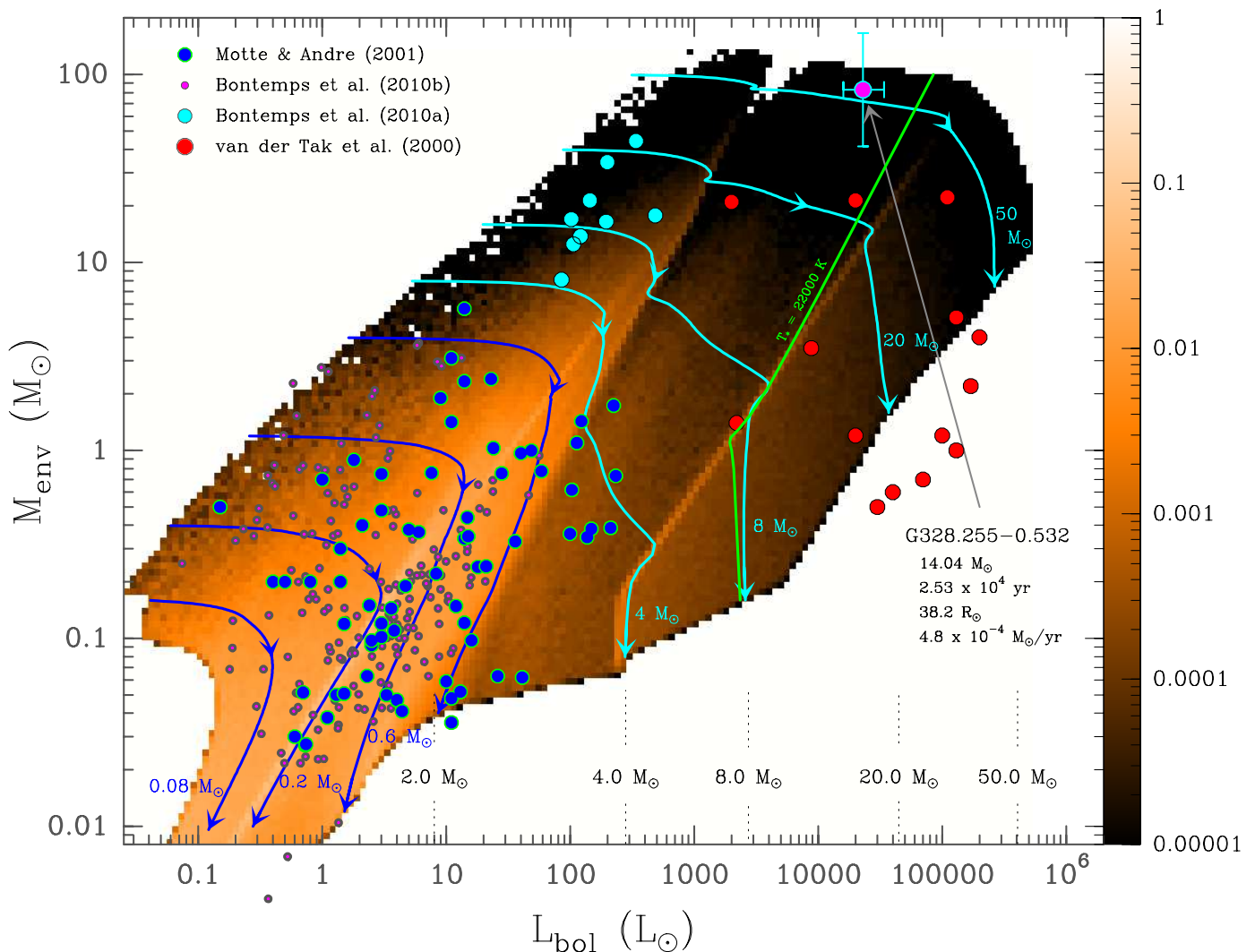
Fig. 10. Evolutionary diagram showing M_{env} versus L_{bol}. The color scale shows the predicted distribution of protostars as a fraction relative to 1 accounting for the typical stellar initial mass function (Kroupa & Weidner 2003) and for a star formation and accretion history (constant star formation and decreasing accretion rates) as described in Duarte-Cabral et al. (2013). (Figure adapted from Motte et al. 2017). The protostar of G328.2551-0.5321 is shown in magenta filled circle.

bulk of the envelope. When looking at the most extreme velocity channels, we find that the emission follows well the azimuthal elongations of the envelope. This gradient is spatially resolved over the blue lobe, that is moving towards our direction and connects the envelope to the compact dust component. The receding arm located on the near side of the envelope is more compact. Altogether this is consistent with a picture of spiral streams developing in the collapsing envelope as the material undergoes infall in a flattened geometry. The development of such spirals is frequently seen in numerical simulations of accretion to a central, dominant protostar. They are typically associated with a flattened structure (e. g. Krumholz et al. 2007; Hennebelle & Ciardi 2009; Kuiper et al. 2011; Hennebelle et al. 2016b). A similar pattern has been observed towards the low-mass sources BHB07-11, in the B59 core Alves et al. 2017, and Elias 2-27 (Pérez et al. 2016); and also on somewhat larger scales of infalling envelopes towards more evolved high-mass star forming regions with an order of magnitude higher luminosity (Liu et al. 2015).

The peak of the torsionally excited state line, together with the ^{13}C isotopologue lines, pinpoint the location of the highest methanol column densities. We explain these observations by two physical components for the CH$_3$OH emission, the more ex-

tended emission associated with the bulk of the inner envelope, and the peak of the $v_t = 1$ line observed at the largest velocity shift compared to the source v$_{lsr}$. In the following we investigate the physical origin of the $v_t = 1$ emission peaks.

Our LTE analysis suggests a high CH$_3$OH column density up to 2×10^{19} cm^{-2} towards these positions, which is at least three orders of magnitude higher than typically observed in the quiescent gas (e.g. Bachiller et al. 1995; Liechti & Walmsley 1997). Such high CH$_3$OH column densities are, however, observed on small scales towards high-mass star forming sites, as reported by e.g. Palau et al. (2017) in the disk component of a high-mass protostar, IRAS20126+4104, and towards other high-mass star forming regions (Beltrán et al. 2014). Towards the hot-cores in the most extreme star forming region, Sgr B2, even higher values are reported above 10^{19} cm^{-2} (Bonfand et al. 2017) .

In particular, the torsionally excited, $v_t = 1$, line with the upper energy level of 315 K, typically requires an infrared radiation field at 20–50 μm in order to populate its upper state. Despite the high average volume densities, assumed to be above $n > 10^7$ cm^{-3}, radiative excitation could be necessary to populate rotational levels in the $v_t = 1$ state. Heated dust in the vicinity of the protostar would naturally provide the infrared photons, there-
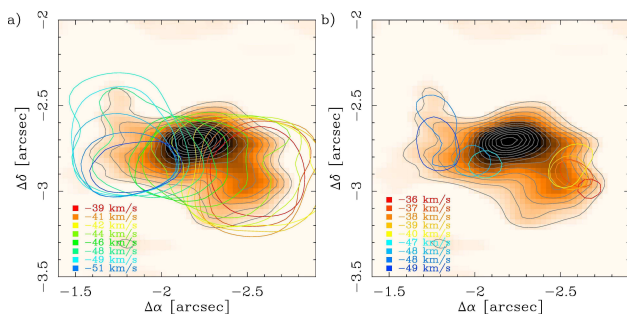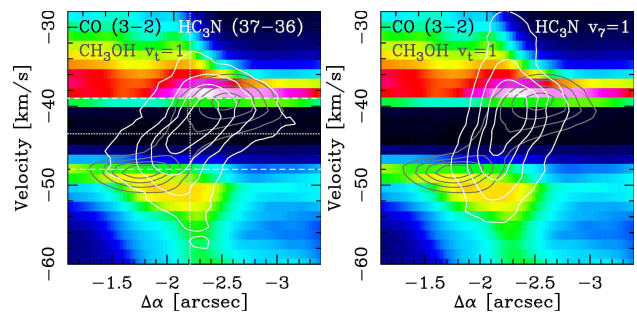
Fig. 11. *a)* The color scale is the same as in Fig. 2*c* showing the thermal dust emission with the larger scale core emission removed in order to enhance the structure of the inner envelope. The color lines show the 50% contour of the peak emission of $v_t = 1$ CH$_3$OH line at different velocities starting from -50.5 km s^{-1} (blue) to -38 km s^{-1} (red). The corresponding velocity of every second contour is shown in the figure legend. *b)* Same as the left panel only showing the 90% contours of most extreme velocity components in red and blue. The velocities corresponding to each contour are shown in the figure legend.

Fig. 12. Comparison of the position velocity map along the $\Delta\alpha$ axis and averaged over a region of $\sim 2.5''$. The color scale shows the CO (3–2) emission which is heavily affected by missing spacings and self absorption at the source v_{lsr}. The dark gray contours show the CH$_3$OH $v_t = 1$, white contours the HC$_3$N (37–37) (left), and the HC$_3$N $v_7 = 1$ (right) transitions.

fore, it is very surprising that this line does not peak on the dust continuum at the position of the protostar, instead it peaks on the inner envelope (Fig 4). This particular pattern could be explained by a decrease of CH$_3$OH abundance towards the protostar, and in fact our results in Sect. 3.3.1 suggest somewhat larger CH$_3$OH column densities offset from the dust peak. Considering that the H$_2$ column density increases towards the continuum peak, and since in Sect. 3.2.2 we rule out optical depth effects of the discussed transitions, this suggests a decreasing CH$_3$OH abundance towards the position of the protostar. The observed high CH$_3$OH column densities and their emission peak could also pinpoint local heating from shocks, which would naturally lead to an increase both in the temperature and in the molecular abundance, especially for CH$_3$OH. This is because CH$_3$OH has been found to show an increase in abundance by orders of magnitude in various shock conditions as the molecule gets released from the grain surfaces via sputtering (Flower et al. 2010; Flower & Pineau des Forêts 2012).

Shocks are produced in a discontinuity in the motion of the gas, and in a collapsing envelope they can emerge in various conditions. One possibility is an origin associated with the outflowing gas hitting the ambient medium of the envelope. Such an increase in the CH$_3$OH abundance has been observed in both low- (Bachiller et al. 1995) and high-mass star forming regions (Liechti & Walmsley 1997; Palau et al. 2017). We therefore compare in more detail the kinematics of the CH$_3$OH emission in Fig. 12 with that of outflow tracers (see Sect. 3.4.2) to exclude its association with outflow shocks. While the CO (3–2) emission is not useful for velocities below $v_{lsr} \pm 6$ km s^{-1} due to strong self absorption, the HC$_3$N $v_7 = 0$ line shows a velocity gradient starting at a position close to the protostar and shows increasing velocities at larger distances. The ± 4.5 km s^{-1} peaks of the CH$_3$OH $v_t = 1$ line are offset from the HC$_3$N $v_7 = 0$ transition, showing no evidence for the CH$_3$OH emission to follow the high-velocity emission from the outflowing gas.

Interestingly, a comparison with the HC$_3$N $v_7 = 1$ line (Fig. 12, right panel), shows that the higher excitation gas is more compact, and is well confined between the spatial and velocity axes outlined by CH$_3$OH. The velocity gradient across the line is visible, its peak is, however, offset from the CH$_3$OH peaks. This supports a picture where the CH$_3$OH and HC$_3$N trace different components, the former one tracing more the inner enve-

lope, while the HC$_3$N $v_7 = 1$ line probes the regions closer to the protostar.

Another possibility to explain the methanol peaks would be the launching of the outflow that would also lead to shocks liberating CH$_3$OH into the gas phase. The launching mechanism of the outflowing gas is highly unexplored territory in high-mass star formation, the location of the outflow launching site is therefore not constrained. Towards low-mass protostars, methanol has been observed to be associated with the launching of the jet/disk wind in the close vicinity, within < 135 au distance from the protostar (Leurini et al. 2016), which is a considerably smaller scale than probed by our observations. There is some indication that towards low-mass protostars outflow can be launched at the outer regions of the Keplerian accretion disk, a recent study of a low-mass Class I type protostar presents an example where the outflow is launched at a distance beyond the disk edge, from the inner envelope (Alves et al. 2017). With our current angular resolution we do not probe such small scales, which would be unresolved, and peaking on the protostar. However, we cannot exclude that the observed CH$_3$OH spots may have contribution from the surface of the flattened envelope.

Given the extent of the torsionally excited CH$_3$OH emission, the best explanation for our observations is that a significant amount of CH$_3$OH is liberated into the gas phase by shocks associated with the inner envelope itself. Around the low-mass Class 0 protostar, L1157, CH$_3$OH has been detected tracing shocks within the infalling gas (Goldsmith et al. 1999; Velusamy et al. 2002). In both of the latter two scenarios explaining the CH$_3$OH emission, the observed maximum velocity offset corresponds to the line-of-sight rotational velocity of the gas at the innermost regions of the envelope.

4.3. Indirect evidence for a Keplerian disk

The brightest spots of the torsionally excited methanol emission can be interpreted as tracing shocks emerging in the innermost regions of the envelope, hence associated with the centrifugal barrier. This happens when the inflowing material from the envelope hits material with a smaller radial velocity component that corresponds to an accretion disk surrounding the central protostar. Such a transition between the envelope and the disk material at the centrifugal barrier has been directly observed in nearby low-mass protostars (Sakai et al. 2014; Oya et al. 2016; Alves et al. 2017). Towards these objects both the gas kinematics and the gas chemistry change at the inner envelope; some studies interpret the extent of this region as a sharp

(c.f. Alves et al. 2017), while others as a more gradual transition region (Oya et al. 2016). Here we observe it as a more extended emission, which also appears to be asymmetric.

Direct evidence for the presence of the disk is hindered by the angular and spectral resolution of our dataset; however, putting all pieces of evidence together, we find several indications supporting the scenario of accretion shocks at the centrifugal barrier. In Sect. 3.1 we already noted a marginally resolved, compact dust component that could correspond to the disk with a resolved major axis of 250 au seen in projection. The elongation of this residual is resolved, and is perpendicular to the outflow axis within ~10°. Both its orientation and extent are consistent with the location of the two CH_3OH peaks at a projected distance of 300 to 800 au considering the uncertainty resulting from our angular resolution of ~400 au.

In addition, we find that the highest excitation molecular emission observed by us in the vibrationally excited HC_3N $v_7 = 1$ line, is very compact, peaking on the compact dust component. This transition has an upper level energy of 645 K, and also requires an infrared radiation field at 20–50 μm in order to populate its vibrationally excited states. Therefore, it more likely traces a region considerably closer to the protostar than the torsionally excited methanol line. Although this molecule is also present in the outflow, as suggested by the vibrationally ground state transition, we propose that the high excitation vibrationally excited HC_3N $v_7=1$ emission is a good candidate for tracing emission from the accretion disk.

Because the accretion disk is expected to be in Keplerian rotation, we can compare the observed pv-diagrams with a simple toy model adapted from Ohashi et al. (1997) to describe an axisymmetric rotating thin disk for the HC_3N $v_7=1$ line, and a ring of gas at the centrifugal barrier for the CH_3OH $v_t = 1$ line (Fig. 13). We show here two models: the CH_3OH lines trace the rotating envelope with $v_{rot}(r) \sim r^{-1}$, and the HC_3N $v_7 = 1$ line traces the gas in Keplerian motion.

We use an x,y grid size of 2×2500 au, and a velocity axis with 0.7 km s^{-1} resolution, a power-law density distribution with $n \propto r^{-1.5}$, constant molecular abundance with respect to H_2, and a central protostellar mass of 15 $M_\odot$ (see Sect 4.1). For the geometry of the CH_3OH emission we use a ring between 300 and 900 au corresponding to the extent of the marginally resolved compact component, and $v_{rot}=4.5$ km s^{-1} at the inner radius of 300 au. For the HC_3N $v_7 = 1$ line, we use a Keplerian model with a disk size up to 600 au.

The models are shown in Fig. 13 for the ring (top row) and the disk (bottom row) component. The observed spots of CH_3OH corresponding to the highest column densities are reasonably well reproduced with these models, the observed asymmetries in the distribution of the emission and projection effects are, however, not included in our models. We break the degeneracy between the location of the ring of CH_3OH emitting gas and the mass of the central object by measuring the position of the methanol shocks. Since we do not include a correction for the inclination angle between the source and our line of sight, the determined parameters are uncertain within a factor of a few.

These models demonstrate that the CH_3OH emission can be well explained by a ring of emitting gas from the infalling envelope that is more extended than the observed HC_3N $v_7 = 1$ line, and the compact dust continuum source. This scenario is similar to what has been observed towards the high-mass object, AFGL2591, by Jiménez-Serra et al. (2012), who find a ring of CH_3OH emission at a velocity that is consistent with the Keplerian velocity of the estimated source mass of 40 $M_\odot$. Due to the observed asymmetry of the HC_3N $v_7 = 1$ line, and our poor
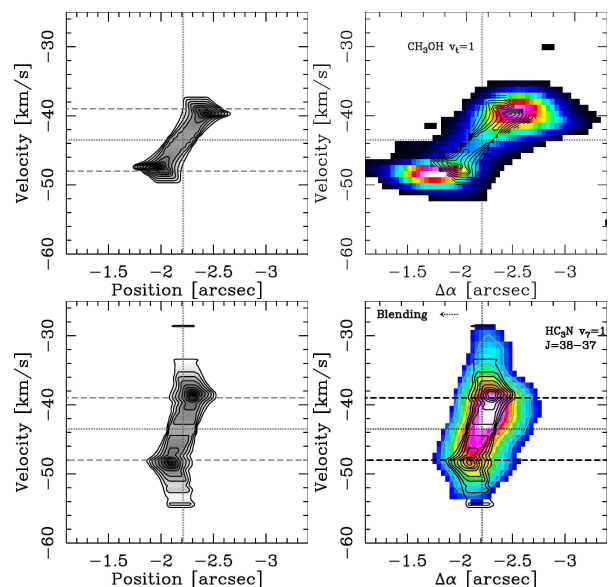
Fig. 13. *Left column:* pv-diagram of models with a rotating ring with $v_r \sim r$ (top), and with a disk in Keplerian rotation (bottom). *Right column:* The color scale shows the 0th moment maps for the 334.42 GHz CH_3OH $v_t = 1$ line (top), and the 346.456 GHz HC_3N $v_7 = 1$ line (bottom). Contours are the same as in the left column and show the model prediction.
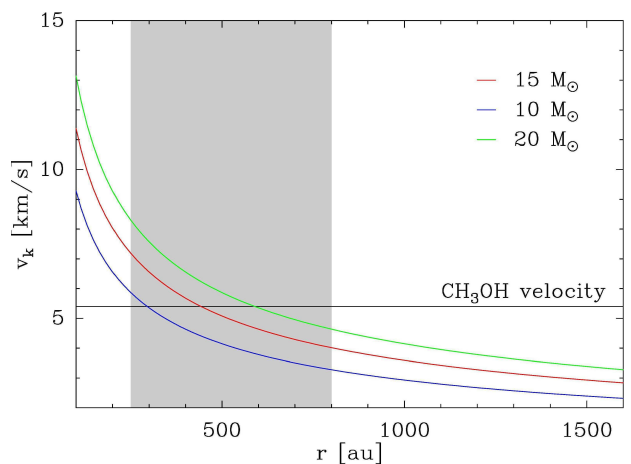
Fig. 14. Keplerian velocity as a function of radius, r, from the central object for 10, 15, and 20 $M_\odot$. The projection corrected velocity determined from the 334.42 GHz CH_3OH $v_t = 1$ line is marked as a gray horizontal line. The grey shaded area corresponds to the projected distance range for the position of the CH_3OH $v_t = 1$ spots.

velocity resolution, our models only show that the extent of the observed velocity range of the HC_3N $v_7 = 1$ line could be consistent with a disk in Keplerian rotation based on the physical constraints of the model.

Finally, in Fig. 14 we show analytic estimates for the Keplerian velocity at a range of central mass between 10 and 20 $M_\odot$, and a range of centrifugal barriers around 300-800 au, which corresponds to the parameter range that could still be consistent with the observations. To obtain the rotational velocity at this radius, we correct the observed 4.5 km s^{-1} for an inclination angle, i, of 56° based on the axis ratio of the measured envelope size in Sect. 3.1. We see that the observed velocity offset of the CH_3OH peaks fits well the Keplerian velocity for the plausible mass range and the range of centrifugal barrier within a resolution element.

4.4. Physical properties of disks around high-mass protostars

Although massive rotating toroids towards precursors of OB-type stars have been frequently detected (Beltrán et al. 2004; Cesaroni et al. 2014; Beltrán et al. 2014; Sánchez-Monge et al. 2013b; Cesaroni et al. 2017), clear signatures of accretion disks around high-mass protostars are still challenging to identify, in particular towards the precursors of the most massive, O-type stars (Beltrán & de Wit 2016). Our results suggest the presence of an accretion disk around a still deeply embedded young high-mass protostar that is likely to be a precursor of an O4-O5 type star. Our findings suggest that a disk may have formed already at this early stage, providing observational support to numerical simulations which predict that despite the strong radiation pressure exerted by high-mass protostars, accretion through flattened structures, and disks enable the formation of the highest mass stars (Krumholz et al. 2009; Kuiper et al. 2010, 2011).

Together with other examples of envelope-outflow-disk systems (e.g. Johnston et al. 2015; Beltrán & de Wit 2016), this suggests a physical picture of high-mass star formation on the core scale that is qualitatively very similar to that of low-mass objects. As observed towards L1527 (Sakai et al. 2014), TMC-1 (Aso et al. 2015), and VLA1623A (Murillo et al. 2013), we also see evidence for shocks induced by the infall from the envelope to the disk imposing a change in the chemical composition of the infalling gas at the centrifugal barrier (see also Oya et al. 2017). The accretion disk around the protostar of L1527 has been confirmed since then with direct imaging (Sakai et al. 2017).
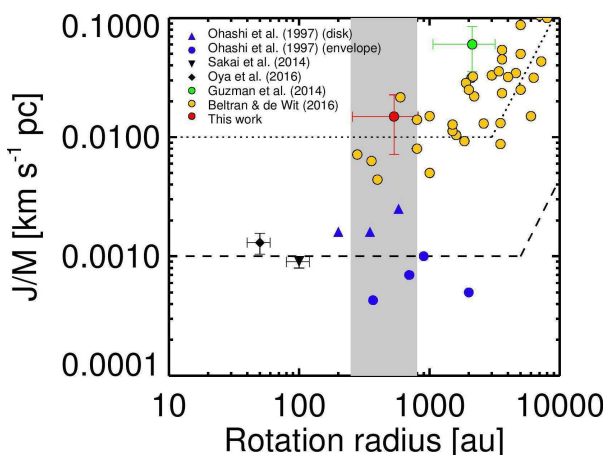
Fig. 15. Local specific angular momentum ($j/m = R \times v_{\rm rot}$) as a function of radius for a sample of low- and high-mass protostars and YSOs. The high-mass sample (Guzmán et al. 2014; Beltrán & de Wit 2016) corresponds to high-mass YSOs with disk candidates, the low-mass objects (Ohashi et al. 1997; Sakai et al. 2014; Oya et al. 2016) correspond to envelopes and disks identified around low-mass Class 0 protostars. Where no explicit information was available, we adopt a 50% uncertainty for the rotation radius, and a linearly propagated 50% uncertainty on the estimated specific angular momentum. For our target, we estimate a 52% uncertainty on these values based on the uncertainty in the disk radius estimate. On this plot we made no attempt to correct for the source's inclination angle. Dashed line shows the j=0.001 km s^{-1} line (Belloche 2013), and an angular velocity, Ω=1.8 km s^{-1} pc^{-1}. For the high-mass sample we show the j=0.01 km s^{-1} pc^{-1} line, and Ω=50 km s^{-1} pc^{-1}. The grey shaded area shows our range of disk size estimate.

Our findings suggest, however, considerably different physical conditions and chemical environment for high-mass protostars. The observed prominent bright peak of CH$_3$OH, that

we explain by shocks at the centrifugal barrier, blends with the more diffuse emission from the envelope. At our spatial resolution, these shocks do not outline a sharp boundary, and leave us with a relatively large range of disk radii that is still consistent with the observations. Based on the size of the compact dust continuum source, we measure a minimum projected radius of ~250 au for the disk major axis, while a maximum outer radius is constrained by the peak of the CH$_3$OH emission located somewhere between 300 and 800 au. We correct these values for an orientation angle of ϕ ~12° based on the fitted position angle of the dust residual emission, giving a disk radius between 255 and 817 au, that is a factor of few larger than recent ALMA observations suggest for disks around some low-mass Class 0 protostars (e.g. Oya et al. 2016; Sakai et al. 2017). For the rotational velocity at this outer radius we take the velocity offset of the CH$_3$OH peaks corrected for the inclination angle (Sect. 4.2). Taking an average disk size between the minimum and maximum expected values implies that the local specific angular momentum, $j/m = R \times v_{\rm rot} = 4.5 \times 10^{21}$ cm^2 s^{-1}, where R is the disk radius, and $v_{\rm rot}$, is the rotational velocity of the disk at the given radius.

We compare our measurement in Fig. 15 to values from the literature following Ohashi et al. (1997), and Belloche et al. (2002), and complement it with high-mass disks and toroids from Beltrán & de Wit (2016). We recognise that the local specific angular momentum is considerably higher towards the high-mass case compared to the low-mass case, although the so far observed disk candidates are still at larger physical scales, and typically towards objects that are likely in a more evolved stage than the protostar of G328.2551-0.5321. This suggests that the kinetic energy may be larger at the onset of the collapse in the case of high-mass star formation. The larger kinetic energy could be explained if the collapse sets in at the clump, thus at >0.3 pc scales compared to the core-scale collapse that is typical for the formation of low-mass protostars. The large specific angular momentum towards high-mass protostars is therefore in agreement with the scenario of global collapse or models based on cloud-cloud collisions at the origin of high-mass stars.

A dust based mass estimate for the disk is very uncertain, not only due to the uncertainty of the temperature, but also because of the unknown dust opacity. Assuming the same dust parameters as for the envelope, and taking $T_{\rm dust}$ = 150 K, we obtain sub-solar mass estimations around $M_{\rm disk} < 0.25\,M_\odot$. Such an elevated temperature is expected for the disk in the close vicinity of the protostellar embryo, it is, however, still consistent with the SED because of the large optical depth of the cooler dust. Since our disk mass estimate is sub-solar, it is likely that the disk mass is below 10% of the mass of the central object and thus gravitationally stable. The stability of the disk itself is an important question, unstable massive disks could either lead to episodic accretion bursts, or undergo fragmentation (Vorobyov & Basu 2010). Both phenomena are observed towards low-mass protostars; in particular multiplicity within low-mass cores has been recently explained by disk fragmentation (Tobin et al. 2016). On the other hand, the high-mass disk candidate AFGL 4176 (Johnston et al. 2015) is more extended, but also more massive. Fragmentation of massive or unstable disks and toroids around high-mass stars could explain why short period binaries have the highest frequency among O-type stars (Sana 2017).

4.5. Implications for high-mass star formation

The fact that we observe at the same time a massive core which is not fragmented down to our resolution limit of ~400 au, and find

strong evidence for a centrifugal barrier at a large radius of 300-800 au, may appear contradictory and needs to be discussed. The observed indication for the Keplerian disk together with the large angular momentum suggest that magnetic braking has not been efficient to evacuate and redistribute the angular momentum. Numerical simulations predict that, in particular, at the early phase of the collapse, the angular momentum from the accretion disk can be efficiently removed due to magnetic braking, and thereby suppress the formation of large disks (e.g. Seifried et al. 2011; Myers et al. 2013; Hennebelle et al. 2016a). Our observations therefore point to a relatively weak magnetic field. On the other hand, despite its large mass which is two orders of magnitude larger than the thermal Jeans mass, the core did not fragment and appears to be collapsing monolithically, which is consistent with the Turbulent Core model (McKee & Tan 2003). This would require additional support to complement the thermal pressure which can either be magnetic or turbulent. Neither the line widths, nor the large angular momentum are consistent with strong enough turbulence or magnetic fields, therefore the properties of the core embedded in G328.2551-0.5321 appear difficult to explain.

However, if turbulence or strong ordered motions are present, the misalignment between the magnetic field lines and the angular momentum vectors can limit the effect of magnetic braking leading to a less efficient removal of the angular momentum (Myers et al. 2013). Alternatively, the present day properties of the collapsing core and the physical state of the pre-stellar core prior to collapse may have been significantly different at onset of the collapse. The small scale properties of high-mass protostars, and the physical properties of their accretion disk, such as in G328.2551-0.5321 may thus challenge high-mass star formation theories. Clearly, more observational examples of accretion disks around high-mass protostars are needed to put further constrains on the formation and properties of disks, and the collapse scenario.

5. Summary and conclusions

We presented a case study of one of the targets from the SPARKS project, which uses high angular-resolution observations from ALMA to study the sample of the most massive mid-infrared quiet massive clumps selected from the ATLASGAL survey. Our observations reveal a single massive protostellar envelope associated with the massive clump, G328.2551-0.5321. Based on protostellar evolutionary tracks, we estimate the current protostellar mass to be between 11 and 16 $M_\odot$, surrounded by a massive core of $\sim$120 $M_\odot$. The estimated envelope mass is an order of magnitude larger than the currently estimated protostellar mass, making this object an excellent example of a high-mass protostar in its main accretion phase, similar to the low-mass Class 0 phase.

We discovered torsionally excited CH_3OH spots offset from the protostar with a velocity offset of ± 4.5 km s^{-1} compared to the source v_{lsr}. These peaks are best explained by shocks from the infalling envelope onto the centrifugal barrier. Based on the observed unblended methanol transitions, we estimate the physical conditions on these spots, and find $T_{kin} = 160 - 170$ K, and $N(CH_3OH) = 1.2 - 2 \times 10^{19}$ cm^{-2}, suggesting large CH_3OH column densities.

Our analysis of the dust emission reveals azimuthal elongations associated with the dust continuum peak, and a compact component with a marginally resolved beam deconvolved $R_{90\%}$ radius of $\sim$250 au measured along is major axis. This component is consistent with an accretion disk within the centrifugal barrier

outlined by the CH_3OH shock spots at a distance between $\sim$300 and 800 au offset from the protostar. Furthermore, we propose the vibrationally excited HC_3N $v_7 = 1e$ J=38–37 line as a potential new tracer for the emission from the accretion disk.

Our results allow for the first time to dissect a clearly massive protostellar envelope potentially forming an O4-O5 type star. The physical picture is qualitatively very similar to that of the low-mass star formation process, however, quantitatively both the physical and the chemical conditions show considerable differences. Our estimate of the specific angular momentum carried by the inner envelope at its transition to an accretion disk is an order of magnitude larger than that observed around low-mass stars. This is consistent with the scenario of global collapse, where the larger collapse scale would naturally lead to a larger angular momentum compared to the core collapse models.

References

Alves, F. O., Girart, J. M., Caselli, P., et al. 2017, A&A, 603, L3
André, P., Ward-Thompson, D., & Barsony, M. 2000, Protostars and Planets IV, 59
Aso, Y., Ohashi, N., Saigo, K., et al. 2015, ApJ, 812, 27
Bachiller, R., Liechti, S., Walmsley, C. M., & Colomer, F. 1995, A&A, 295, L51
Belloche, A. 2013, in EAS Publications Series, Vol. 62, EAS Publications Series, ed. P. Hennebelle & C. Charbonnel, 25–66
Belloche, A., André, P., Despois, D., & Blinder, S. 2002, A&A, 393, 927
Beltrán, M. T., Cesaroni, R., Neri, R., & Codella, C. 2011, A&A, 525, A151
Beltrán, M. T., Cesaroni, R., Neri, R., et al. 2004, ApJ, 601, L187
Beltrán, M. T., Cesaroni, R., Neri, R., et al. 2005, A&A, 435, 901
Beltrán, M. T. & de Wit, W. J. 2016, A&A Rev., 24, 6
Beltrán, M. T., Sánchez-Monge, Á., Cesaroni, R., et al. 2014, A&A, 571, A52
Benjamin, R. A., Churchwell, E., Babler, B. L., et al. 2003, PASP, 115, 953
Beuther, H., Schilke, P., Menten, K. M., et al. 2002, ApJ, 566, 945
Bonfand, M., Belloche, A., Menten, K. M., Garrod, R. T., & Müller, H. S. P. 2017, A&A, 604, A60
Bontemps, S., Andre, P., Terebey, S., & Cabrit, S. 1996, A&A, 311, 858
Bontemps, S., Motte, F., Csengeri, T., & Schneider, N. 2010, A&A, 524, A18
Carey, S. J., Noriega-Crespo, A., Mizuno, D. R., et al. 2009, PASP, 121, 76
Cesaroni, R., Galli, D., Neri, R., & Walmsley, C. M. 2014, A&A, 566, A73
Cesaroni, R., Sánchez-Monge, Á., Beltrán, M. T., et al. 2017, A&A, 602, A59
Csengeri, T., Bontemps, S., Wyrowski, F., et al. 2017a, A&A, 601, A60
Csengeri, T., Bontemps, S., Wyrowski, F., et al. 2017b, A&A, 600, L10
Csengeri, T., Leurini, S., Wyrowski, F., et al. 2016, A&A, 586, A149
Csengeri, T., Urquhart, J. S., Schuller, F., et al. 2014, A&A, 565, A75
Cutri, R. M., Wright, E. L., Conrow, T., et al. 2012, Explanatory Supplement to the WISE All-Sky Data Release Products, Tech. rep.
Duarte-Cabral, A., Bontemps, S., Motte, F., et al. 2013, A&A, 558, A125
Dunham, M. M., Crapsi, A., Evans, II, N. J., et al. 2008, ApJS, 179, 249
Flower, D. R. & Pineau des Forêts, G. 2012, MNRAS, 421, 2786
Flower, D. R., Pineau Des Forêts, G., & Rabli, D. 2010, MNRAS, 409, 29
Garay, G., Mardones, D., Bronfman, L., et al. 2010, ApJ, 710, 567
Goldsmith, P. F., Langer, W. D., & Velusamy, T. 1999, ApJ, 519, L173
Gómez, L., Wyrowski, F., Pillai, T., Leurini, S., & Menten, K. M. 2011, A&A, 529, A161
Guzmán, A. E., Garay, G., & Brooks, K. J. 2010, ApJ, 725, 734
Guzmán, A. E., Garay, G., Rodríguez, L. F., et al. 2014, ApJ, 796, 117
Hennebelle, P. & Ciardi, A. 2009, A&A, 506, L29
Hennebelle, P., Commerçon, B., Chabrier, G., & Marchand, P. 2016a, ApJ, 830, L8
Hennebelle, P., Lesur, G., & Fromang, S. 2016b, A&A, 590, A22
Hosokawa, T. & Omukai, K. 2009, ApJ, 691, 823
Hosokawa, T., Yorke, H. W., & Omukai, K. 2010, ApJ, 721, 478

Jiménez-Serra, I., Zhang, Q., Viti, S., Martín-Pintado, J., & de Wit, W.-J. 2012, ApJ, 753, 34

Johnston, K. G., Robitaille, T. P., Beuther, H., et al. 2015, ApJ, 813, L19

Kroupa, P. & Weidner, C. 2003, ApJ, 598, 1076

Krumholz, M. R., Klein, R. I., & McKee, C. F. 2007, ApJ, 656, 959

Krumholz, M. R., Klein, R. I., McKee, C. F., Offner, S. S. R., & Cunningham, A. J. 2009, Science, 323, 754

Kuiper, R., Klahr, H., Beuther, H., & Henning, T. 2010, ApJ, 722, 1556

Kuiper, R., Klahr, H., Beuther, H., & Henning, T. 2011, ApJ, 732, 20

Langer, W. D. & Penzias, A. A. 1990, ApJ, 357, 477

Leurini, S., Codella, C., Cabrit, S., et al. 2016, A&A, 595, L4

Liechti, S. & Walmsley, C. M. 1997, A&A, 321, 625

Liu, H. B., Galván-Madrid, R., Jiménez-Serra, I., et al. 2015, ApJ, 804, 37

Lumsden, S. L., Hoare, M. G., Urquhart, J. S., et al. 2013, ApJS, 208, 11

Maret, S., Hily-Blant, P., Pety, J., Bardeau, S., & Reynier, E. 2011, A&A, 526, A47

McKee, C. F. & Tan, J. C. 2003, ApJ, 585, 850

Milam, S. N., Savage, C., Brewster, M. A., Ziurys, L. M., & Wyckoff, S. 2005, ApJ, 634, 1126

Molinari, S., Brand, J., Cesaroni, R., & Palla, F. 2000, A&A, 355, 617

Molinari, S., Schisano, E., Elia, D., et al. 2016, A&A, 591, A149

Molinari, S., Swinyard, B., Bally, J., et al. 2010, PASP, 122, 314

Moscadelli, L., Sánchez-Monge, Á., Goddi, C., et al. 2016, A&A, 585, A71

Motte, F., Bontemps, S., & Louvet, F. 2017, ArXiv e-prints [arXiv:1706.00118]

Motte, F., Bontemps, S., Schilke, P., et al. 2007, A&A, 476, 1243

Mottram, J. C., Hoare, M. G., Urquhart, J. S., et al. 2011, A&A, 525, A149

Murillo, N. M., Lai, S.-P., Bruderer, S., Harsono, D., & van Dishoeck, E. F. 2013, A&A, 560, A103

Myers, A. T., McKee, C. F., Cunningham, A. J., Klein, R. I., & Krumholz, M. R. 2013, ApJ, 766, 97

Ohashi, N., Hayashi, M., Ho, P. T. P., & Momose, M. 1997, ApJ, 475, 211

Ossenkopf, V. & Henning, T. 1994, A&A, 291, 943

Oya, Y., Sakai, N., López-Sepulcre, A., et al. 2016, ApJ, 824, 88

Oya, Y., Sakai, N., Watanabe, Y., et al. 2017, ApJ, 837, 174

Palau, A., Fuente, A., Girart, J. M., et al. 2013, ApJ, 762, 120

Palau, A., Walsh, C., Sánchez-Monge, Á., et al. 2017, MNRAS, 467, 2723

Peretto, N., Fuller, G. A., Duarte-Cabral, A., et al. 2013, A&A, 555, A112

Pérez, L. M., Carpenter, J. M., Andrews, S. M., et al. 2016, Science, 353, 1519

Phillips, C. J., Norris, R. P., Ellingsen, S. P., & McCulloch, P. M. 1998, MNRAS, 300, 1131

Purser, S. J. D., Lumsden, S. L., Hoare, M. G., et al. 2016, Monthly Notices of the Royal Astronomical Society, 460, 1039

Rosero, V., Hofner, P., Claussen, M., et al. 2016, ApJS, 227, 25

Sakai, N., Oya, Y., Higuchi, A. E., et al. 2017, MNRAS, 467, L76

Sakai, N., Sakai, T., Hirota, T., et al. 2014, Nature, 507, 78

Sana, H. 2017, ArXiv e-prints [arXiv:1703.01608]

Sánchez-Monge, Á., Cesaroni, R., Beltrán, M. T., et al. 2013a, A&A, 552, L10

Sánchez-Monge, Á., Cesaroni, R., Beltrán, M. T., et al. 2013b, A&A, 552, L10

Sanna, A., Surcis, G., Moscadelli, L., et al. 2015, A&A, 583, L3

Schöier, F. L., van der Tak, F. F. S., van Dishoeck, E. F., & Black, J. H. 2005, A&A, 432, 369

Schuller, F., Menten, K. M., Contreras, Y., et al. 2009, A&A, 504, 415

Seifried, D., Banerjee, R., Klessen, R. S., Duffin, D., & Pudritz, R. E. 2011, MNRAS, 417, 1054

Sridharan, T. K., Beuther, H., Schilke, P., Menten, K. M., & Wyrowski, F. 2002, ApJ, 566, 931

Tanaka, K. E. I., Tan, J. C., & Zhang, Y. 2017, ApJ, 835, 32

Tobin, J. J., Kratter, K. M., Persson, M. V., et al. 2016, Nature, 538, 483

Urquhart, J. S., Busfield, A. L., Hoare, M. G., et al. 2007, A&A, 461, 11

Velusamy, T., Langer, W. D., & Goldsmith, P. F. 2002, ApJ, 565, L43

Vorobyov, E. I. & Basu, S. 2010, ApJ, 719, 1896

Wyrowski, F., Güsten, R., Menten, K. M., et al. 2016, A&A, 585, A149

Wyrowski, F., Güsten, R., Menten, K. M., Wiesemeyer, H., & Klein, B. 2012, A&A, 542, L15

Zhang, Q., Hunter, T. R., Brand, J., et al. 2005, ApJ, 625, 864

[1] Max-Planck-Institut für Radioastronomie, Auf dem Hügel 69, 53121 Bonn, Germany e-mail: csengeri@mpifr-bonn.mpg.de
[2] OASU/LAB-UMR5804, CNRS, Université Bordeaux, allée Geoffroy Saint-Hilaire, 33615 Pessac, France
[3] INAF - Osservatorio Astronomico di Cagliari, Via della Scienza 5, I-09047 Selargius (CA), Italy
[4] Max Planck Institute for Astronomy, Königstuhl 17, 69117 Heidelberg, Germany
[5] Departamento de Astronomía, Universidad de Chile, Casilla 36-D, Santiago, Chile
[6] Univ. Lyon, ENS de Lyon, Univ Lyon1, CNRS, Centre de Recherche Astrophysique de Lyon UMR5574, F-69007, Lyon, France
[7] IRAM, 300 rue de la piscine, 38406, Saint-Martin-d'Héres, France
[8] Astrophysics Research Institute, Liverpool John Moores
[9] Instituto de Radioastronomía y Astrofísica, Universidad Nacional Autónoma de México, P.O. Box 3-72, 58090, Morelia, Michoacán, México
[10] Dept. of Space, Earth & Environment, Chalmers University of Technology, Gothenburg, Sweden
[11] Dept. of Astronomy, University of Virginia, Charlottesville, VA, USA
[12] School of Physical Sciences, University of Kent, Ingram Building, Canterbury, Kent CT2 7NH, UK

## Appendix A: Dust spectral energy distribution and modelling

We construct the spectral energy distribution (SED) of the protostar embedded in the clump G328.2551-0.5321, from the mid-infrared wavelengths up to the radio regime (Fig. A.1) in order to estimate its bolometric luminosity (L_{bol}), and constrain a representative dust temperature (T_d) for the bulk of the mass using a model of greybody emission.

In Fig. A.1 we show the flux densities from the GLIMPSE catalog at the shortest indicated wavelengths (Benjamin et al. 2003), as well as the WISE band 4 photometry at $22\,\mu$m (Cutri et al. 2012). To illustrate the complexity of the region, we show the emission from the far-infrared and millimetre wavelength range in Fig. A.2 using Herschel/Hi-GAL data (Molinari et al. 2010), and the ATLASGAL-Planck combined data at $870\,\mu$m (Csengeri et al. 2016). This shows that the emission is largely dominated by extended structures at all these wavelengths.

As a comparison we show the corresponding sources identified in the Herschel/Hi-GAL point source catalog (Molinari et al. 2016), and the ATLASGAL Gaussclumps source catalog (Csengeri et al. 2014). The $870\,\mu$m flux density measurement by ALMA reveals the MDC at a size-scale of 0.06 pc (see also Csengeri et al. 2017b) and therefore puts constraints on the extent of the embedded source. To derive therefore the properties of the gas representative of the embedded protostar, our aim is to extract and scale the flux densities corresponding to a source at $\sim 8''$ (the geometric mean of the PACS $70\,\mu$m beam, Molinari et al. 2016) with a density profile of $n \sim r^{-2}$, and neglecting any temperature gradient. To do this, we perform aperture photometry on the PACS $70\,\mu$m, and $160\,\mu$m maps by first measuring the peak intensity at the position of our target within a single beam (taking $5.8''\times12.1''$, and $11.4''\times13.4''$, respectively), and then measure the background emission in 3 different annuli at increasing distance from $15''$ to $35''$ with respect to the source. For the SPIRE 250, 350, and $500\,\mu$m data, we use the values from the Herschel/Hi-GAL point source catalog, and scale them adopting the geometric mean of the measured major and minor axes (Molinari et al. 2016).

To obtain the bolometric luminosity of the protostar, we add up all emission from the near/mid-infrared to $870\,\mu$m, and obtain $1.3 \times 10^4 \, L_{bol}$. As a comparison, we also calculated the protostar's internal luminosity using the empirical relation between L_{bol} and the flux density measured at $70\,\mu$m (Dunham et al. 2008), and obtain $1.2 \times 10^4 \, L_{bol}$. The significant confusion due to extended emission from the mid-infrared to the submillimeter wavelengths adds, however, some uncertainty to our estimate, the measured values likely correspond to an upper limit to the luminosity.

To obtain an estimate of the dust temperature, T_d, we perform a greybody fit to the far-infrared points of the SED between $70\,\mu$m and $870\,\mu$m. Since at $70\,\mu$m the emission is mostly dominated by the heated dust in the vicinity of the protostar, we use a two component greybody to model the SED, which reveals the temperature corresponding to the cold gas component dominating the bulk of the emission, and puts strong constrain on the warm gas temperature, as well as the fraction of the heated gas mass. We use $\kappa_{345\,GHz} = 0.0185\,\mathrm{g\,cm^{-2}}$ and an emissivity index of $\beta = 2$, where $\kappa_\nu = \frac{\nu}{345\,GHz}^{-\beta}$. We obtain a cold gas component at 22 K, and a warm gas component at 48 K that contains <5% of the total gas mass. The result of the SED fit is shown in Fig. A.1.
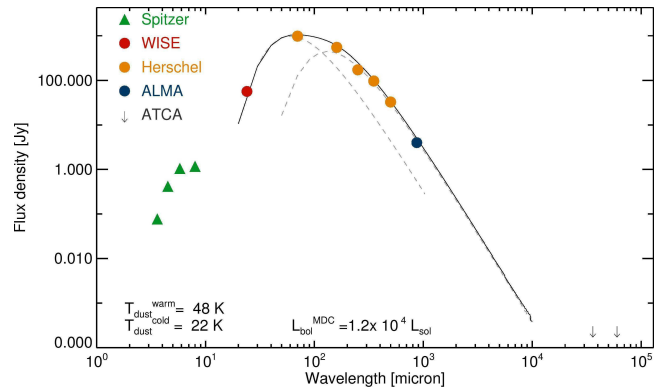
Fig. A.1. SED of the embedded protostar within the ATLASGAL clump, G328.2551-0.5321. The origin of the shown flux densities are labeled in the figure legend, and are described in the text. Solid line shows the result of a two (warm and cold) component grebody fit with 48 K and 22 K. The individual components are shown in a dashed gray line.
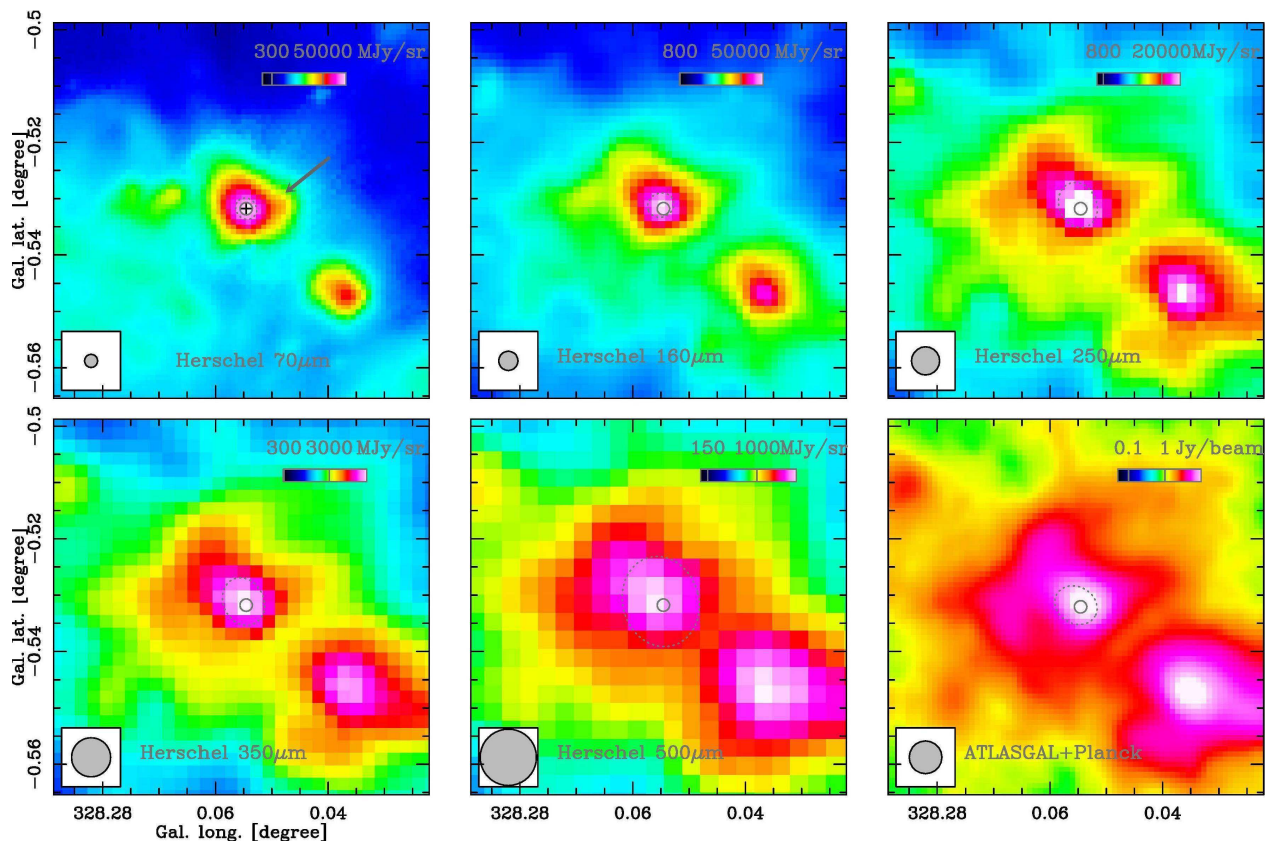
Fig. A.2. Far-infrared multi-wavelength view of the ATLASGAL clump, G328.2551-0.5321 using the *Herschel* Hi-GAL images (Molinari et al. 2016), and the APEX/LABOCA and Planck combined maps (Csengeri et al. 2016). The position of the identified source is marked with a black cross, dotted gray ellipses show the corresponding sources from the Hi-GAL, and ATLASGAL catalogues (Molinari et al. 2016; Csengeri et al. 2014, respectively). The solid circle shows half the 8″ *FWHM* corresponding to the scale of the MDC. The FWHM beam widths are shown in the lower left corner of each panel. The color scale goes on a logarithmic scale, the black line shows the labeled flux density value.